SERA
Seismology and Earthquake Engineering
Research Infrastructure Alliance for Europe

DELIVERABLE

D24.5 Analysis of network performance for investigations of earthquake statistics

Work package	WP24
Lead	CNRS
Authors	D. Bindi (GFZ) M. Campillo (CNRS) F. Cotton (GFZ) J. Kokowski (IGPAS) D. Schorlemmer (GFZ) M. Sobiesiak (IGPAS) Ł. Rudziński (IGPAS)
Reviewers	-
Approval	Management Board
Status	Final
Dissemination level	Public
Delivery deadline	30.04.2020
Submission date	30.04.2020
Intranet path	DOCUMENTS/DELIVERABLES/SERA_D24.5_Analysis_network_performance.pdf

This project has received funding from the European Union's Horizon 2020 research and innovation programme under grant agreement No 730900.

Contents

1. Introduction

National or regional networks provide the necessary seismic data for studies in the respective regions. Contrary to global networks, regional networks achieve much higher completeness levels for various types of analyses, among them spatial and temporal statistical analyses and seismic hazard studies. In this deliverable, we address the problem of national and regional network performance and the influence of the network characteristics (geometry, instrumentation) on the physical and statistical understanding of earthquake process.

This analysis is performed at various scales:

- At the European scale, we test the consistency of ML magnitude evaluation using the data collected by national networks. We analyze in a consistent way the regional variation of wave attenuation, compare them with the one used at the national level and finally compute a harmonized Local Magnitude scale at the scale of the continent. This study has given the opportunity to detect in a systematic way the errors of European seismological ways inventories. This development is the first step toward a consistent development of a consistent ML earthquake catalogue at the European scale.
- At the national scale, we take advantage of a well-documented track of the operational status of each station of the Greek (NOA) seismological network to analyze the time-dependencies of the Greek catalogue completeness and the ability of the network to detect small earthquakes.
- At the regional scale, we evaluate the ability of dense regional network to evaluate the physical properties of small earthquake (e.g. stress-drop). Such analysis is performed in one of the best instrumented part of Europe (central Italy)
- We finally evaluate the possibility of supporting the daily routine catalogue with additional detections and locations from the software developed in the other SERA WP24 tasks (e.g. PyMPA) to a network installed to monitor the seismicity of a mine (LUMINEOS network)

The conclusion summarizes the lessons learned by these analyses for future European seismological network developments. These analyses benefited also from the discussions and developments described in the deliverables D4.6 and D4.7.

2. Analysis of network performance at the European scale: Toward European Magnitude computations (Bindi et al. 2019a, 2019b)

2.1. Motivation

Technological developments of the last twenty years that affected both the communication infrastructures and monitoring equipment, had also a strong impact on our ability to make large volume of seismological data accessible by a wide community. Nowadays, most of the seismic observatories acquire, archive and disseminate in real-time high-resolution multi-channel streams provided by monitoring systems ranging from near fault observatories to global networks. The introduction of standards for both seismological data format (https://ds.iris.edu/ds/nodes/dmc/data/formats/seed/) and dissemination services (http://www.fdsn.org/about/) has allowed easy access to data to be turned into scientific developments. An example is the European Integrated Data Archive (EIDA, http://www.orfeus-eu.org/data/eida/), an open-access infrastructure where data acquired by different European networks are archived and disseminated following common international standards. The possibility to access data acquired by different networks using the same standards, along with the open source development of libraries for data mining and processing, allows to develop harmonized seismological models on large spatial scale which, in turn, support the investigation of regional dependencies of source and propagation effects.

Here, we take advantage of the dense and high quality data collected across Europe to derive a harmonized local magnitude scale without network or political boundaries (Bindi et al. 2019a, 2019b). Several factors motivated the development of a local magnitude scale for the European continent using a documented and modern technique, such as the possibility to complement amplitude readings and unify catalogues from different seismic networks, particularly for earthquakes occurring close to the national boundaries. Moreover, it would facilitate the empirical conversions between local and moment magnitudes when creating seismic catalogues for hazard assessment purposes. Finally, it would allow to investigate and account for region-dependent features affecting the attenuation in different tectonic regions of Europe.

2.2. Data, networks and processing

We compiled the data set of waveforms, and associated metadata, necessary to develop the harmonized European magnitude scale by querying the European Integrated Data Archive (EIDA). EIDA is a federation of data centres which archive and disseminate waveform data and metadata gathered by numerous European research infrastructures, using standard FDSN services. To access, download and pre-processing the waveforms, we used stream2segment (Zaccarelli 2018; Zaccarelli et al. 2019), a Python package designed for helping the user in the whole workflow of downloading, inspecting and processing event-based seismic data. Stream2segment allows to create a relational data base (e.g. PostgreSQL or SQLite) where the segments extracted from the continuous data streams are stored along with their parametric information. The extraction of segments from continuous data streams is guided by a seismic catalogue compiled, in this study, using the event-webservice of the European Mediterranean Seismological Centre (EMSC). Among other parameters, the earthquake selection criteria include the selection of the geographical region of interest for the hypocentral locations, the time frame including the origin times, the magnitude and depth ranges. The configuration file also defines parame-

ters for searching contributing stations (e.g., a magnitude-dependent hypocentral distance filter), selection of specific networks or stations of interest, which channels have to be downloaded, the duration of the extracted segments. For an exhaustive description of stream2segments, see Zaccarelli et al. (2019).

For the application presented here, we searched stations within a radius of 3° from the epicentres of events with magnitude smaller than 3.5, within a radius of 6° for magnitudes larger than 5.5, and a linear interpolation over the distances is applied for magnitudes in-between. Only events with depth shallower than 50 km and recorded by public accessible networks were considered. From each stations, we downloaded segments 4 min long, starting 1 min before the theoretical first P-wave arrival time, requesting all available streams with a minimum sampling rate of 50 Hz. We downloaded segment mainly for channels HH, EH, HN (or HG, HL). More detailed information are available in Bindi et al. (2019a). The data base of downloaded segments includes ~4.5 million segments retrieved from 11 data centres and relevant to ~50 thousand earthquakes recorded by ~10 thousand stations belonging to ~200 networks. We considered both permanent and temporary installations with the only requirements that data were fully open (restricted or under embargo data were ignored). Figure 1 summarizes the performances about the download process, showing in a map view which are the stations contributing to the data base. The symbol size is proportional to the total number of requested segments and the intensity of the red colour depends on the percentage of received segments with respect to the total requested. The statistics can be broken at the level of the single data centre and the performances with respect to different communication errors can be inspected by the user. As shown by Figure 1, we considered several different networks in Europe, including the major national and regional networks (e.g. CH, IV, GR, HL, FR, KO, IB, BS, OE, SK, SL, NS, among many others) but also temporary installations deployed in the framework of different projects. The harmonization of the data format and the possibility of following standards for data discovery and download allow us to process all these networks as a single European network.

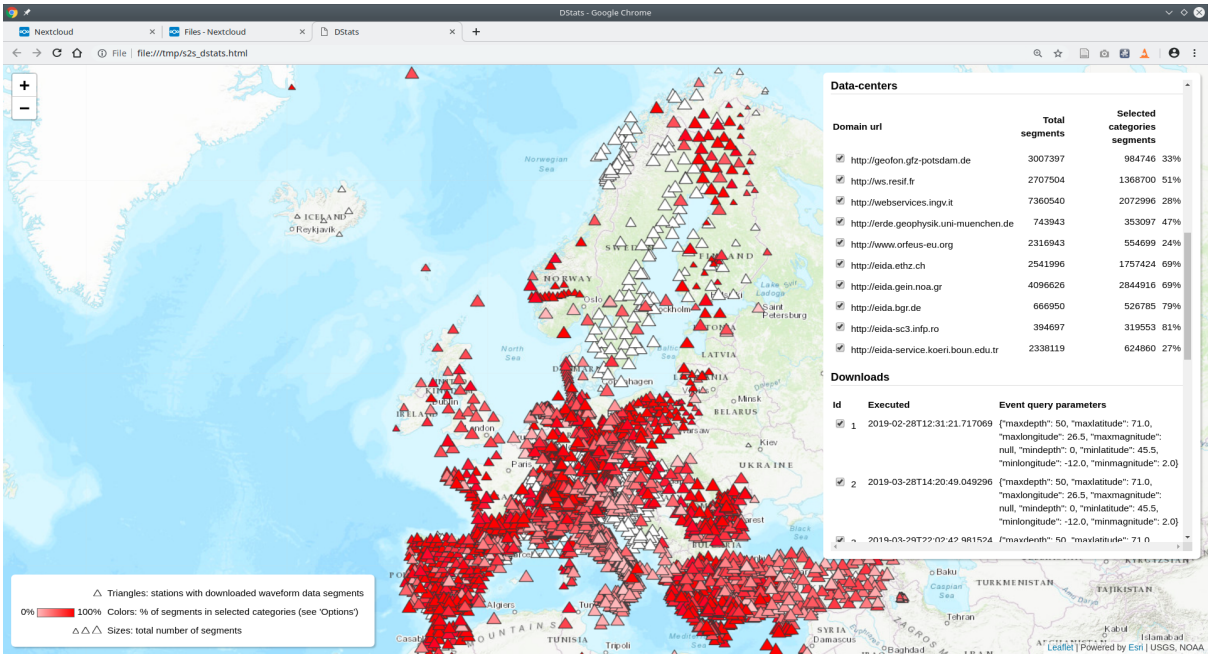

Figure 1. Summary of the segments downloaded from 11 different data centres. Triangles indicate the location of contributing stations with symbol size proportional to the number of requests and the intensity of the red colour informative for the percentage of provided segments with respect to the total number requested. The interactive map allows the user to select which are the data centres of interest and to customize the displayed information (e.g., which segments corresponding to specific communication errors). White triangles indicate stations which did not provide any requested segment (restricted data).

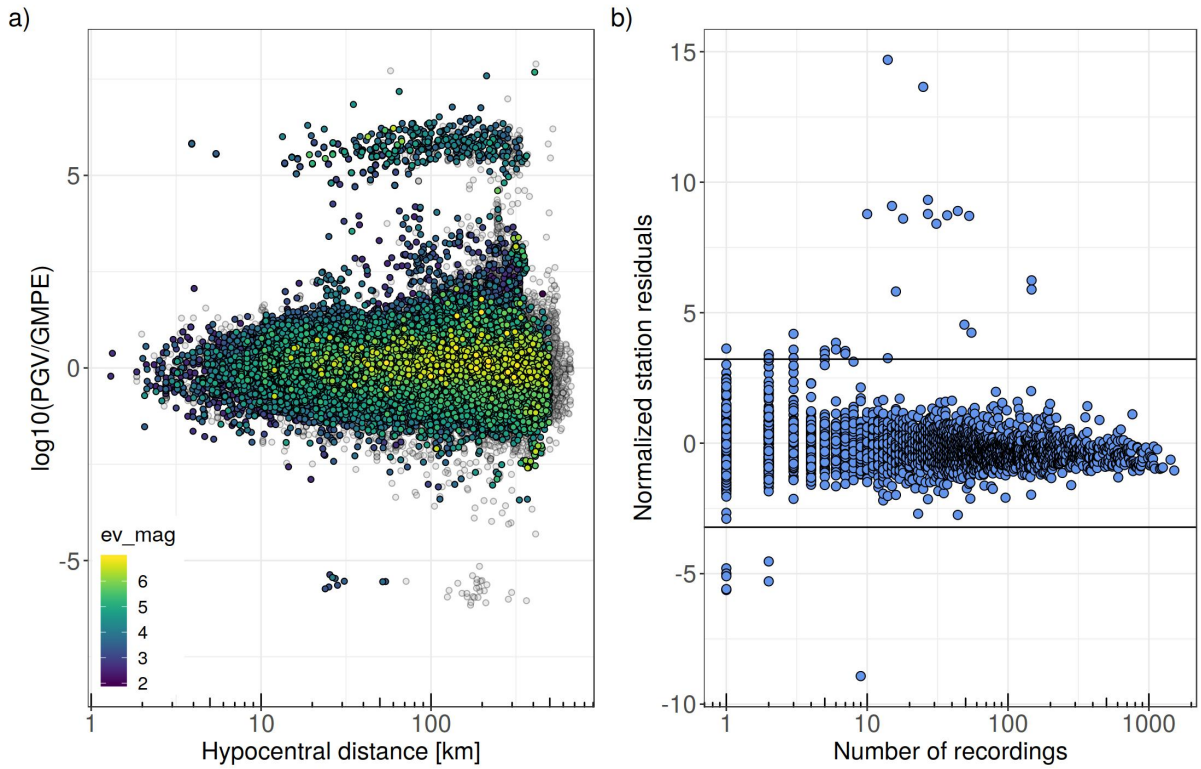

Figure 2. Example of residual analysis performed to identify stations with atypical behaviour (in the following, also referred to as outliers). Panel a) shows the residuals computed for PGV considering the Bindi et al. (2014) ground motion prediction equation; panel b) shows the normalized station-to-station residuals for stations in the analysed data set.

In order to select those segments which are suitable for performing the magnitude calibration, pre-processing analysis were performed in two steps. The first step (QC1) consisted in selecting segments without gaps or overlap, with a percentage of missing data smaller than 50 per cent of the total requested amount, and discarding segments with maximum amplitude exceeding a saturation threshold. An a-causal Butterworth band-pass filter was applied, with high-pass corner selected according to the magnitude retrieved from the EMSC event-catalogue (Bindi et al. 2019a). The instrumental response was removed from the filtered waveform and synthetic Wood-Anderson traces computed considering a static magnification of 2080 and a natural period of 0.8 s. Finally, the geometrical mean of the maximum values over the two horizontal components was considered for developing the local magnitude scale. In the second level of selection (QC2), we evaluated the signal to noise ratio (SNR) over different bandwidths and we investigated the residual distributions for peak ground velocity (PGV) and acceleration (PGA), considering different Ground Motion Prediction Equations (GMPEs). The between-events and the station-to-station residuals (Kotha et al. 2017) were also analysed. Figure 2 exemplifies the PGV residuals, and the relevant station-to-station residuals, obtained considering one specific GMPEs (Bindi et al. 2014). We used the residual distributions to identity stations with atypical results, considered as outliers and not further considered in the analysis. The systematic large residuals obtained for some stations are often related to problems in the metadata retrieved from the station inventories.

As a result of the QC2 selection, from 428000 segments passing QC1 the data set was reduced to 205300 records from 12721 earthquakes. Regarding the stations, 772 channels out of 2812 are from strong motion instruments and co-located sensors were considered during the analysis as different stations. The final data set is shown in Figure 3 in terms of source-to-station path coverage. As expected, areas with the highest station density are concentrate in the Mediterranean region, in particular in Italy,

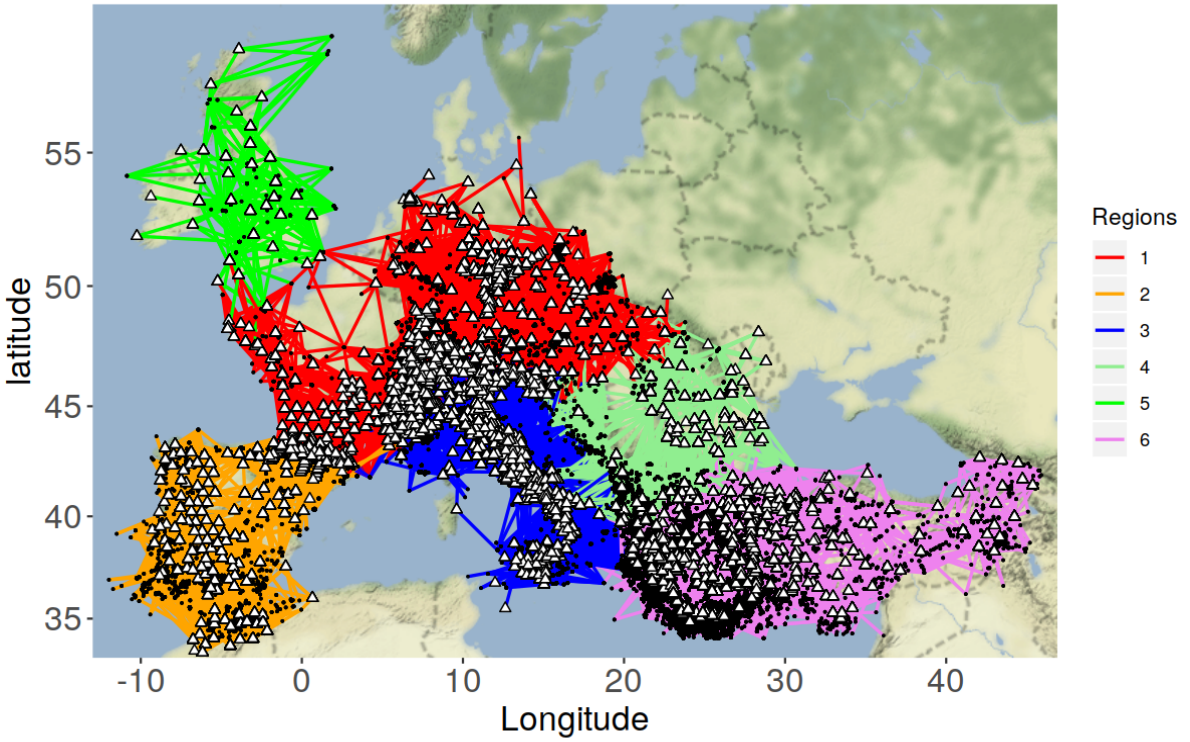

Figure 3. Data set used for calibrating the harmonized local magnitude scale in Europe. Colours indicate the six different areas used to define regional non-parametric attenuation models. White triangles indicate the station locations, black dots the earthquake epicentres.

Greece and Turkey. High density networks are also monitoring Switzerland and the most active areas of France.

Figure 4 quantifies the density of the considered stations by creating the Voronoi diagram over the station location and evaluating the distributions of the cell's areas. Considering the whole analysed data set (top panels), the median area is 684 km^2 which reduces to 327 km^2 considering only Italy and the Alpine area (middle panels). One of the most dense area is central Italy (bottom panels), where the median is 75 km^2 and half of the stations have the first neighbour within 10km.

2.3. Methods

In order to exploit the large data availability, and to connect our results to the standard observatory practice, we applied two-tier approach. In the first level, we calibrated a local magnitude scale following a non-parametric approach (Savage and Anderson 1995, Spallarossa et al. 2002), considering six different regions (Figure 3) to capture the spatial variability of seismic attenuation. The six regions correspond to Central Europe (Region 1), Iberia-Maghreb (Region 2), Central Mediterranean (Region 3), Balkans (Region 4), British Isles (Region 5) and Aegean-Anatolia (Region 6). Due to the small number of recordings in our selected data set, Scandinavia region is not considered in this study. In the second level, the magnitudes obtained in the first layer were used to calibrate a set of parametric attenuation functions with attenuation adjustments for the attenuation at the network level.

2.4. Non-parametric calibration

The non-parametric model is described by

$$logA_{kl}(R) = a_n logA_0^{region}(R_n) + a_{n+1} logA_0^{region}(R_{n+1}) + \sum_{i=1}^{N_{event}} Ml_i\, \delta_{ik} + \sum_{j=1}^{N_{stations}} S_j\, \delta_{jl} \quad (1)$$

where A_{kl} is the logarithm in base 10 of the Wood–Anderson amplitude (measured in mm) of event k recorded at station l. The three distance ranges from 1 to 100 km, from 100 to 200 km, and from 200

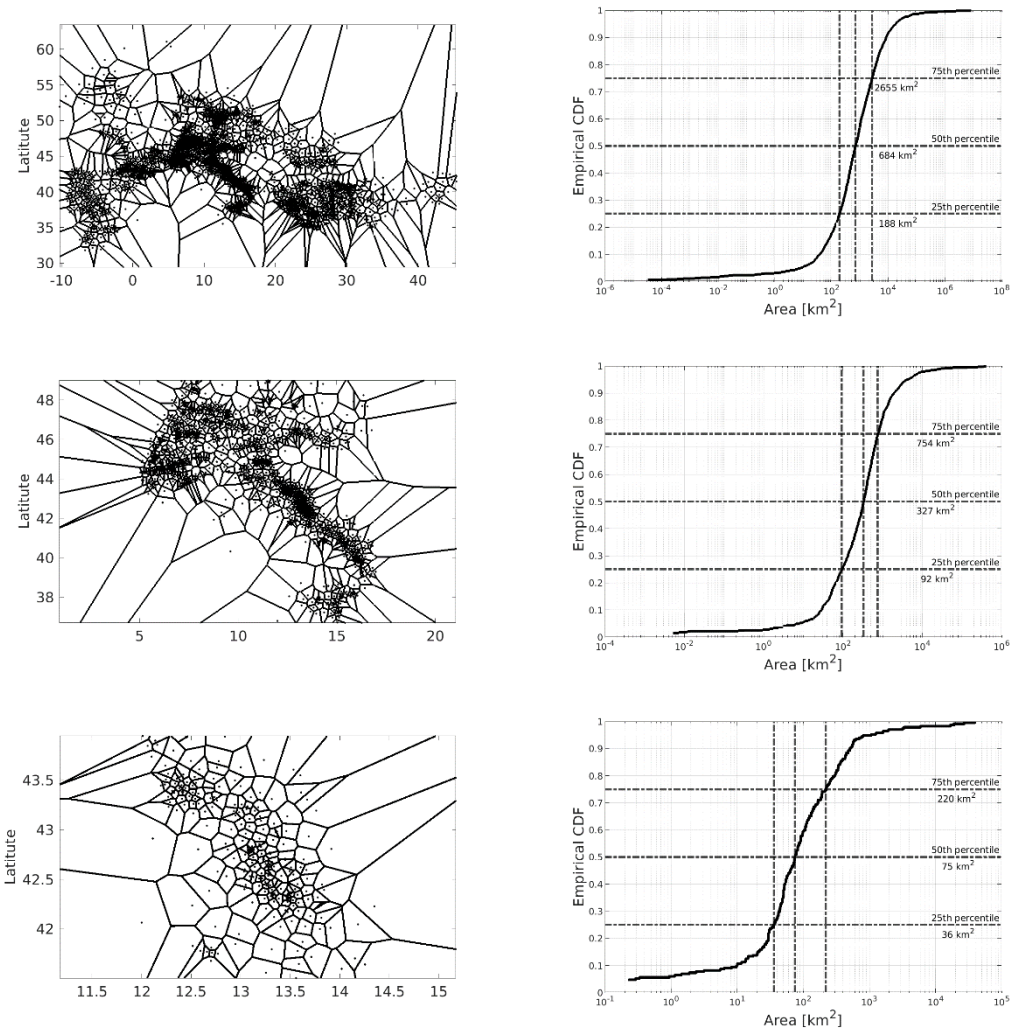

Figure 4. Density of stations measured considering the area of Voronoi's cells. In the left panels, the Voronoi diagrams are constructed at three different spatial scale, from the European scale (top) to central Italy (bottom). In the right panels, the empirical cumulative density functions of the areas are shown and the 25th, 50th, and 75th percentiles are indicated.

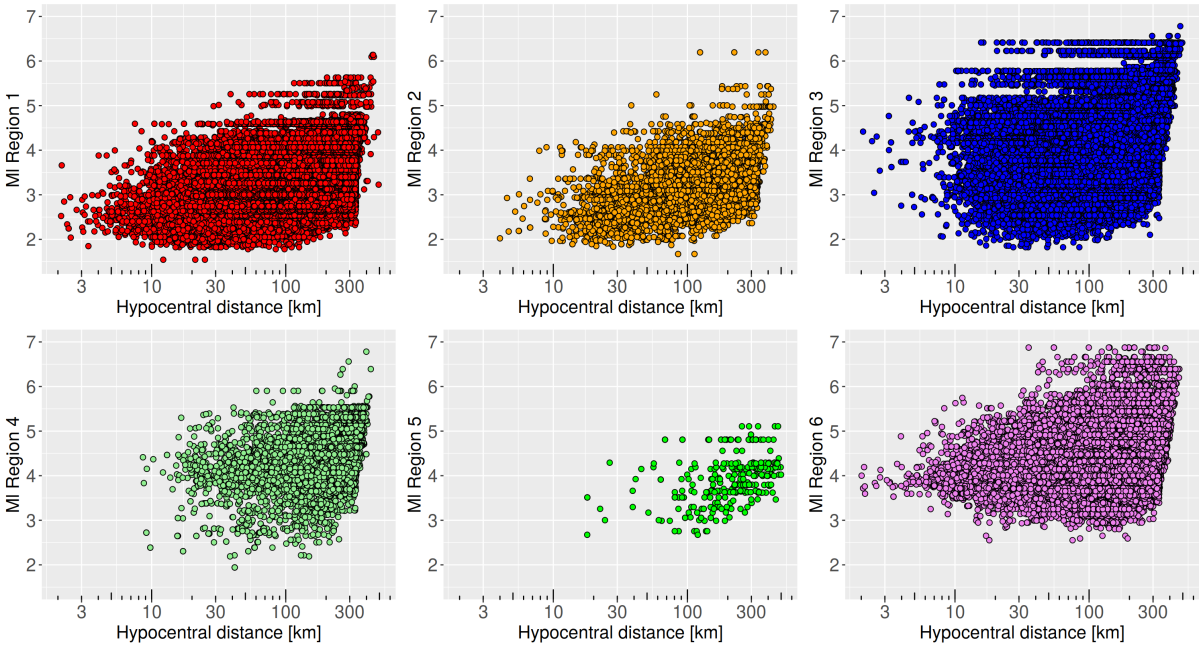

Figure 5. Magnitude versus distance scatterplot for the six regions (as shown in Figure 3) considered to calibrate the non-parametric model of equation (1).

to 400 km are discretized in equal spaced bins 5, 10 and 20 km wide, respectively. In equation (1), R_n, with n = 1, ..., 41, are the nodes separating the distance bins and the hypocentral distance R is such that $R_n \leq R < R_{n+1}$; $a_n = (R_{n+1} - R)/\Delta R$; $\Delta R = (R_{n+1} - R_n)$; $a_{n+1} = 1 - a_n$; δ_{ik} and δ_{jl} are Kronecker deltas that allow the use of dummy variables; Ml_i is the local magnitude of earthquake i; S_j is the station correction of station j; $N_{station}$ and N_{event} are the number of station and earthquakes, respectively. In equation (1), a different non-parametric attenuation model $logA_{0region}$ is calibrated simultaneously for each region, assuming the following constraints: (1) the corrections S_j, j=1,...,N_{ref}, of a set of N_{ref} reference stations sum to zero; (2) the attenuation functions are constrained to $logA_0(17\ km) = -2$ for all regions. As set of reference stations, we used the Italian seismic network (FDSN network code IV). Since IV is a large seismological network contributing to several regions (i.e. regions 1, 3, 4 and 6) and it recorded a large number of earthquakes, its choice as reference led to the most stable inversion results. The linear system in equation (1) was solved in least-squares sense and uncertainties are estimated through bootstrap analysis. For more details, see Bindi et al. (2019a). The scatter plots of the magnitude–distance distribution used for the magnitude calibration are shown in Figure 5.

2.5. Parametric calibration

The magnitudes obtained with the non-parametric approach were used to refine the attenuation models. We applied a parametric approach using a mixed effects approach (e.g., Kotha et al. 2017) with random effects on the attenuation model using the networks as grouping levels (Bindi et al. 2019a). Therefore, a specific parametric attenuation model is calibrated for each single network, resulting in more than 70 different calibrated magnitude scales. This large number of models allow us to compare our results with previously derived scales and to evaluate the between-network variability within the same region or country. The parametric mode is based on a functional form including two attenuation terms, one depending on the logarithm of distance and the other proportional to the distance (Hutton and Boore, 1987):

$$\begin{aligned} log\mathcal{A}(R) = logA - Ml = \\ e_1 + G(n_1, n_2, n_3; log(R), R_a, R_b) + Q(k_1 + \Delta k_1^{net}; k_2 + \Delta k_2^{net}; R, R_a, R_b) + \delta S2S \end{aligned} \quad (2)$$

In equation (2), the logarithm of the Wood–Anderson amplitudes are corrected for the magnitude value Ml obtained through the non-parametric approach. The parametric model includes an offset term (term e_1) and the so-called geometrical spreading G and anelastic attenuation Q terms. The model includes also the random effects Δk_1^{net} and Δk_2^{net} applied to k_1 (distance range from R_a to R_b) and k_2 (distances larger than R_b), respectively, and depending on the network, whereas δS2S are the (magnitude) station corrections evaluated as random effects on the station grouping level. A piece-wise linear geometrical spreading model is considered:

$$G(n_1, n_2, n_3; \log(R), R_a, R_b) = \begin{cases} n_1 \log(R) & \text{if } R \le R_a \\ n_1 \log(R_a) + n_2 \log\left(\frac{R}{R_a}\right) & \text{if } R_a < R \le R_b \\ n_1 \log(R_a) + n_2 \log\left(\frac{R_b}{R_a}\right) + n_3 \log\left(\frac{R}{R_b}\right) & \text{otherwise,} \end{cases} \quad (3)$$

where the slopes n_1, n_2, n_3 are considered as fixed effects and the breakpoints R_a and R_b are fixed at 10 and 60 km in order to capture both the near source attenuation and to describe the attenuation at distances not significantly affected by the effects of secondary arrivals. The anelastic attenuation term Q is modelled as

$$Q(k; R, R_a, R_b) = \begin{cases} 0 & if R \le R_a \\ k_1 (R - R_a)/100 & R_a \le R < R_b \\ k_1 (R_b - R_a)/100 + k_2 (R - R_b)/100 & otherwise, \end{cases} \quad (4)$$

where the parameters k_1 and k_2 are considered as fixed effect.

2.6. Results

Figure 6 compares the non-parametric attenuation functions obtained for the 6 macro areas considered to account for regional differences in the attenuation (Figure 3).

For each region, the distribution of the 500 bootstrap results is compared to the Hutton and Boore (1987) model for southern California (black curves), used as reference model. The bootstrap analysis shows that the data set allows to get stable results for all regions except for the British Isles, which requires additional data to constrain the regional attenuation.

Differences in the attenuation among the regions are evident, the attenuation being strongest in region 6 and weakest in region 2, and reaching a difference of about 0.4 magnitude units (m.u.) at 400 km. Regions 1 and 2 show stronger attenuation than California in the first 60 km about; then, the attenuation curves flatten due to the effect of later arrivals, particular evident in region 1; for distances above 100–120 km, the attenuation rate in these two regions is similar to the California one. Regarding Region 5, the bootstrap attenuation curves show a larger dispersion than for the other regions since a much smaller data set is analysed (Figure 5). Nevertheless, considering the 5th and 95th percentiles of the bootstrap distribution (yellow curves in Figure 6), the trend of the attenuation with distance is similar to Region 1.

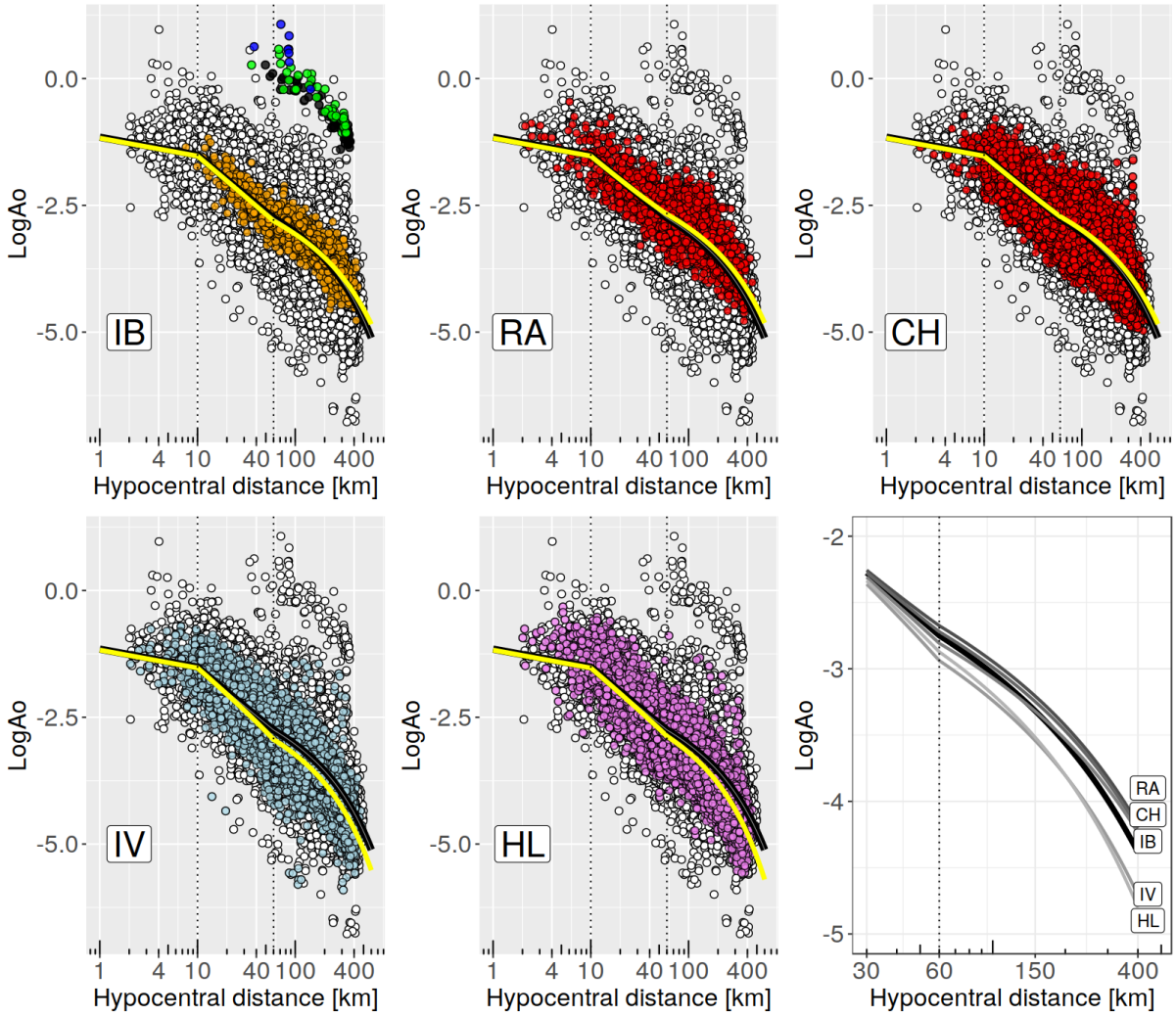

Figure 7. Parametric attenuation models $logA_0$ obtained for five national networks (the FDSN network code is provided inside each panel). The network-dependent models are shown in yellow, the median model (i.e. without considering the network adjustments) in black. The recordings from each network are shown as circles filled according to the region mostly including the network (Figure 3); white circles are data from other networks. In the bottom right-hand panel, the logA0 models are compared for distances above 30 km. In the panel for IB, the black, green and blue circles indicate some outliers recorded at specific stations.

Figure 7 shows the parametric models for selected national networks operating in different regions (the FDSN code of the networks are IB, RA, CH, IV and HL). Data recorded by all networks are shown as white circles whereas those recorded by each specific network are filled with the same colour of the macro region mostly including the network (see Figure 3). In the panel for network IB, some outliers are indicated with black, green and blue circles, corresponding to station JAVS of network SL (channel HH), station KNDS of network SL (channel HH) and station SRO of network SK (channel EH), respectively. In each panel, the attenuation models accounting for the network-dependent adjustments are shown in yellow whereas the model constructed considering only the fixed effects (the same to all networks) is shown in black. The comparison reported in the bottom right frame of Figure 7 highlights the presence of significant regional differences among the attenuation models. Details about the parametric models are available in Bindi et al. (2019a, 2019b).

Figure 8 (left) shows the distribution of the station corrections for the non-parametric models (symbols S in equation 1), grouped by network. We recall that the calibration is performed by constraining the

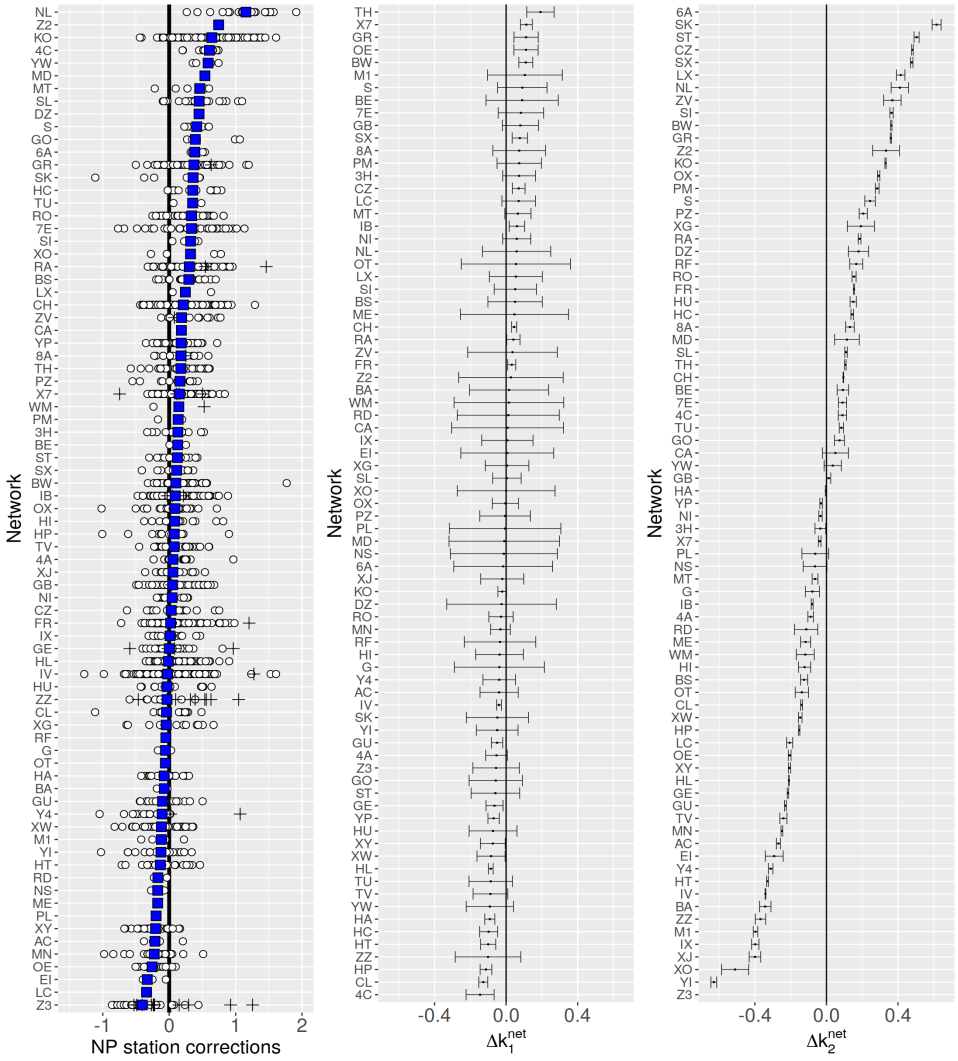

Figure 8. Left. Station corrections for the non-parametric model of equation (1). Results or each station (circles) are grouped by network (FDSN codes are shown as row names) and the average network correction is shown with a blue rectangle. Middle. Network-dependent adjustments Δk_1^{net} for the distance range 10-60 km (equation 2). Right. Network-dependent adjustments Δk_2^{net} for the distances >60 km.

average station correction of the IV network (Italy) to zero. Stations indicated with crosses are characterized by bootstrap standard deviations larger than 0.6 m.u. and they are not further considered. The distribution of the station corrections confirms that local site amplification effects can have a strong impact on ground motion (more than ±1 magnitude units) and contributes significantly on the magnitude residuals variability. One of the most important benefit of having used EIDA to calibrate a harmonized scale is the possibility of using the Wood-Anderson amplitudes, adjusted using consistent magnitude station corrections, from most of the stations in Europe. The network-dependent adjustments Δk_1 and Δk_2 (equation 2) are shown in middle and right panels of Figure 8, respectively. Positive values indicate less attenuation with respect to the median model constructed considering only the fixed effects. The variability among the networks is strongest for k_2, which can be interpreted as connected to anelastic attenuation effects. Regarding k_1, over the 10–60 km distance range, the large standard errors make Δk_1 net significantly different from zero only for few networks. Positive Δk_2 net values are obtained for networks in region 1 (e.g. networks TH, BW, SX, GR, in Germany; CH in Swiss; RA and FR in France); among the negative values, we have HL, HT, HP in Greece, and IV (Italy). Considering large national networks, examples of positive Δk_2^{net} are Δk_2^{GR} = (0.3599 ± 0.0032) (German network, Region

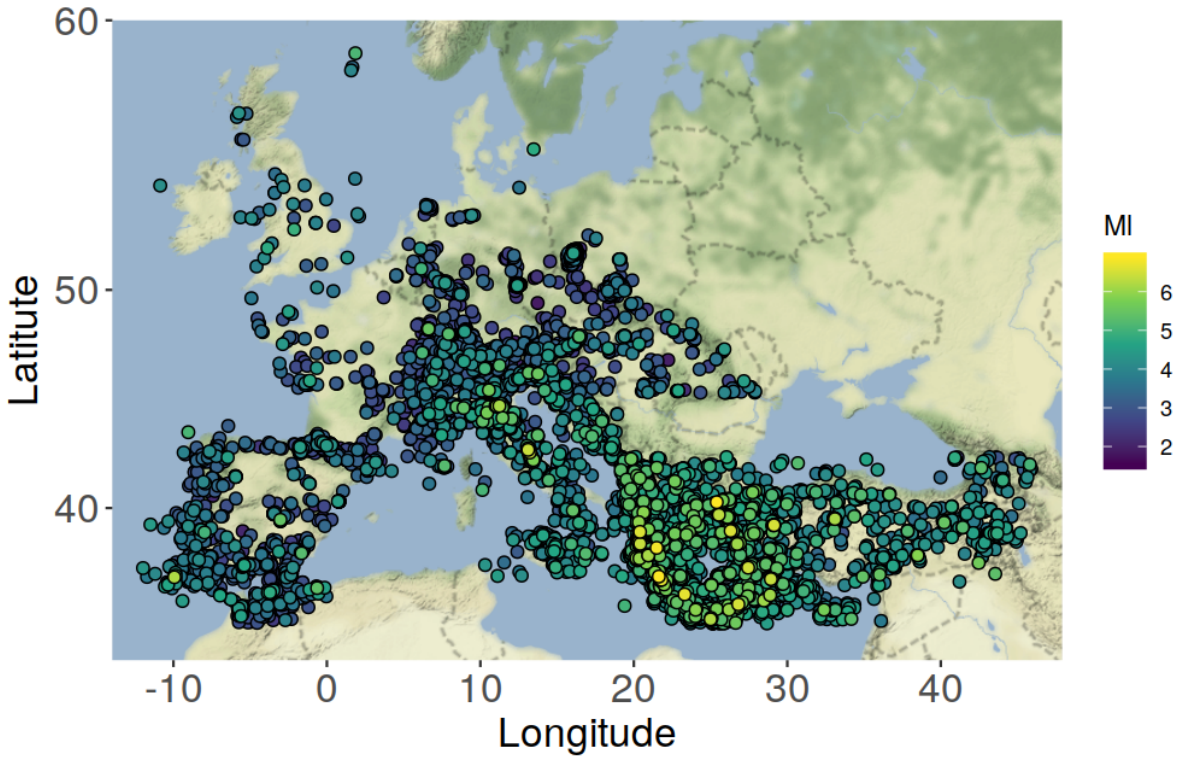

Figure 9. Earthquakes used to derive the harmonized local magnitude scale using the non-parametric approach. Symbols are coloured coded accordingly to the average bootstrap magnitude solution.

1), Δk_2^{KO} = (0.3302 ± 0.0033) (Koeri network in Turkey, Region 6), Δk_2^{FR} = (0.1539 ± 0.0032) (France network, Region 1), Δk_2^{CH} = (0.0946 ± 0.0016) (Swiss network, Region 1); negative Δk_2 net are obtained for Δk_2^{IB} = (−0.0798 ± 0.0054) (Iberian network, Region 2), Δk_2^{HL} = (−0.2097 ± 0.0016) (Greek network, Region 6) and Δk_2^{IV} = (−0.3410 ± 0.0018) (Italian network, Region 3). Finally, the magnitude residuals computed for the parametric model (Bindi et al. 2019a) do not show any trend with distance, even at short distances (Luckett et al. 2018), confirming that the breakpoints at 10 and 60 km allow to capture correctly the changes in the slope of attenuation with distance.

The final catalogue of ~12500 events with harmonized local magnitude is shown in Figure 9, in map view. Note that magnitudes greater than about 6 can be affected by saturation effects due to the Wood–Anderson response. A detailed analysis of the obtained magnitudes and a comparison with existing catalogues will be subject of future research.

2.7. Discussions and conclusion

We took advantage of the European Integrated Data Archive (EIDA) to develop the first harmonized local magnitude scale for central and southern Europe. The main conclusions are the following:

(i) the non-parametric analysis shows that $\log A_0$ has strong regional characteristics within the study area and the rate of attenuation changes significantly over different distance ranges;

(ii) the non-parametric analysis shows that the attenuation for distances smaller than 60 km is stronger than the attenuation predicted by the model for California (Hutton and Boore 1987), causing differences up to 0.3 m.u. at 60 km; for larger distances, $logA_0$ differences exceeding 0.4 m.u. at 400 km are observed among regions in central and southern Europe; moreover, later arrivals have a strong influence on $logA_0$ at distances between 60 and 120 km;

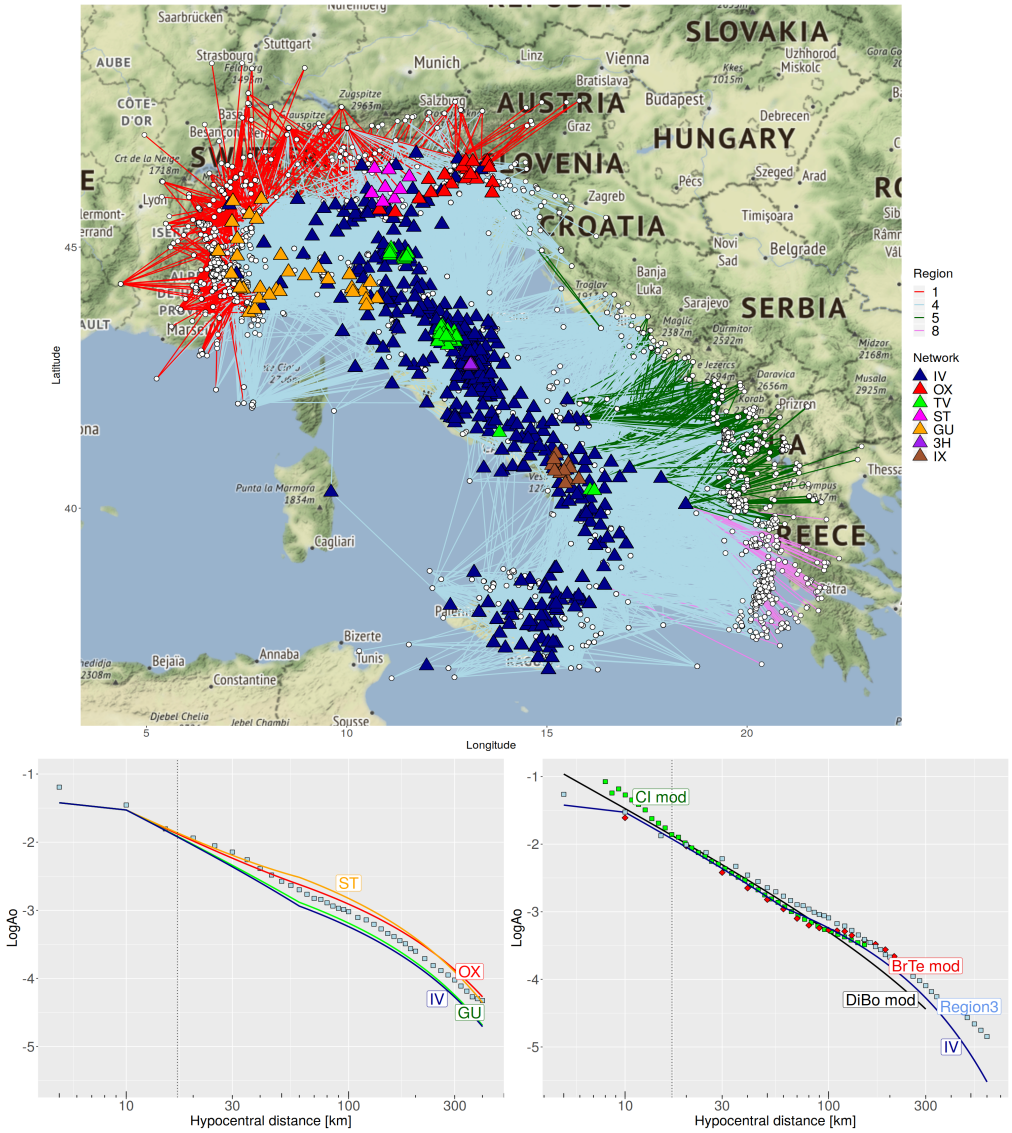

Figure 10. Example of parametric analysis for Italy. The map shows some selected networks, both permanent (e.g. OX, GU) and temporary (e.g. TV, 3H). The considered networks are: IV, Italian National Seismic Network (doi:10.13127/SD/X0FXnH7QfY); ST, Trentino Seismic Network (doi: 10.7914/SN/ST); OX, North-East Italy Seismic Network (doi: 10.7914/SN/OX); GU, Regional Seismic Network of North Western Italy(doi: 10.7914/SN/GU); TV, INGV experiments network; 3H, Norcia basin (Italy) temporary network (doi: 10.14470/8U7554472182); IX, Irpinia Seismic Network. The colours of the source-to-station paths correspond to the regions in Figure 2. Bottom left: the non-parametric attenuation model for region 3 (squares) is compared to the parametric models adjusted for different networks (i.e., ST, OX, IV, GU). Bottom right: the non-parametric model for region 3 (light blue squares) and the parametric model for network IV (blue line) are compared to models derived in previous studies: CI_mod, Bindi et al. (2018), central Italy; BrTe_mod, Bragato and Tento (2005), northeastern Italy; DiBo_mod, Di Bona (2016), for Italy. Original models have been shifted to match at the reference distance of 17 km and no corrections accounting for differences in the Wood-Anderson maximum amplitude definition among the models has been applied.

(iii) considering national seismic networks, the network-dependent adjustments $\Delta k_2^{network}$ applied to the parametric models are negative (stronger attenuation than the median model for distances larger than 60 km) for HL (Greece) and IV (Italy), positive (weaker attenuation) for KO (Turkey), GR (Germany), FR (France) and CH (Swiss); for several countries, the between-network variability among $\log A_0$ functions for networks operating in the same country is within ±0.2 m.u.

In conclusion, the availability of a harmonized magnitude scale makes easier the operation of comparing and merging catalogues provided by different networks and allows to jointly analyse amplitudes recorded at stations belonging to different networks operating in adjacent regions. For example, Figure 10 exemplifies the possibility open by considering a harmonized magnitude scale, in terms of either comparison among models calibrated for different regions of Italy or comparison with models derived in different studies. Future work will look into the ISC Bulletin and comparison between the Ml obtained from the homogenized calibration functions here presented and the reported Ml to the ISC.

3. Analysis of network performance at the national scale: completeness analysis

National or regional networks provide the necessary seismic data for studies in the respective regions. Contrary to global networks, regional networks achieve much higher completeness levels for various types of analyses, among them spatial and temporal statistical analyses and seismic hazard studies. Continuing the series of previous studies about the temporal and spatial evolution of seismic network recording completeness, e.g. for Italy (Schorlemmer et al. 2010), Switzerland (Nanjo et al. 2010), and Japan (Schorlemmer et al. 2018), D. Schorlemmer (GFZ) together with N. Melis (NOA) and K. Lentas (ISC) have conducted a study on the network of the National Observatory of Athens (NOA), Greece. Like in the previous studies, the analysis was carried out using the Probability-based Magnitude of Completeness (PMC) method, as developed by Schorlemmer and Woessner (2008). A publication about this work is in preparation.

Because the recording completeness of every network depends on the distribution of operational stations, the first step in such an analysis is the estimation of operational times of each station over time. Figure 1 shows operational times of a set of NOA stations over the investigation period. It can be seen that most stations were recording only with short interruptions. However, some stations exhibit larger gaps in recording which is reducing the recording possibilities of the network in the area of these stations. In this study, the operational times were assessed based on the average pick frequency of a station, meaning that unreasonably long inter-pick times were considered an off-time of the station. It is important for a network to exactly know the operational times and, hence, networks should keep track of the operational status of each station and document the outages. This analysis would have profited from such a track record. Still, most networks do not keep track of stations outages.

For a full spatio-temporal analysis of the recording capabilities of the NOA network, the probabilities of detecting events were computed for each magnitude at each grid node (0.1 x 0.1 degrees) in the study area of Greece. From these sets of probabilities per node, the completeness magnitude is defined as the lowest magnitude for which the recording probability is 0.99 or larger (99% level). To compute a map of detection probabilities for a point in time, the recording capabilities of each station operational on that very point in time needs to be calculated (Figure 2). This is performed as an empirical analysis

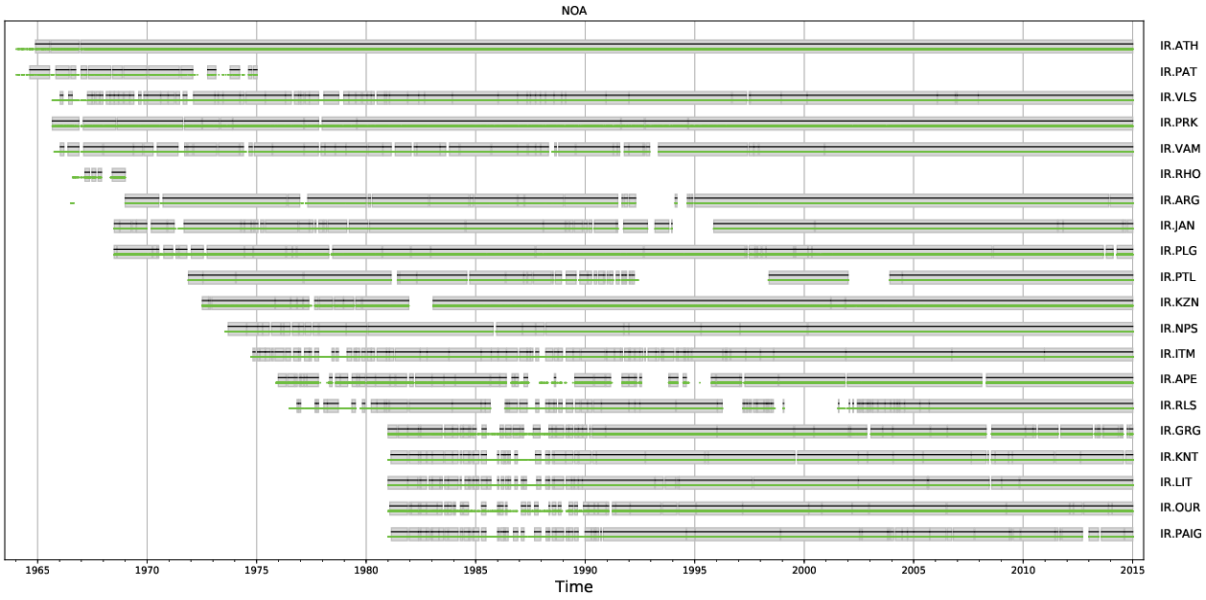

Figure 1. Operational times of a selection of NOA stations. For each station, picks at the respective station are plotted as green points.

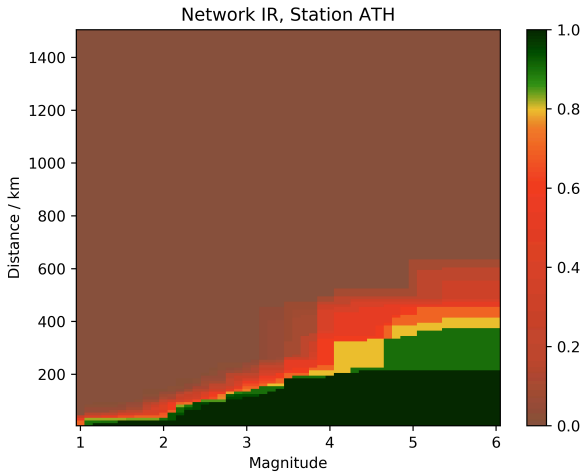

Figure 2. Detection-probability distribution (colour-coded) of station ATH of the NOA network on 1 October 2014. The detection probability is computed for each magnitude (1 to 6 in 0.1 unit steps) and distance (5 km to 1500 km in 5 km steps) based on the recording performance around that date. These distributions are calculated for each station separately.

of the pick performance around that point in time and contains various factors like site conditions, coupling of the station, station characteristics etc.

The development of the NOA network and its recording capabilities of particularly small-magnitude earthquakes can be seen in Figure 3. While the network was not able to detect magnitude 1.5 events in the 1980s, the capabilities were increased in the 1990s in the area around Thessaloniki by installing more stations with smaller inter-station distance than in the remaining parts of Greece. This trend continued in the 2000s with more and more stations being installed in on the Peloponnese peninsula later on the Aegean islands. This expansion of station coverage and its increasing station density resulted in a significantly improved network capable of reliably detecting magnitude 1.5 events in almost all parts of Greece.

A similar picture is presented in the completeness maps (Figure 3). While the network was not even able to reliably detect events of magnitude 3 in all of Greece during the 1980s, the 1990s showed a strong improvement in the Thessaloniki area where the completeness level dropped to M_P = 2 and below while the mainland of Greece reached completeness of approx. M_P = 3. The subsequent deployment of new stations resulted in a completeness of approx. M_P = 1.5 in almost all parts of Greece.

This analysis, like the aforementioned analyses in other regions, document the quality improvements of the investigated networks. Several lessons have been learned from these analyses:

- Temporal losses of completeness due to station outages should be detected and documented by the networks. In the classical completeness estimates based on the Gutenberg-Richter (G-R) relation, time-limited drops in recording capabilities will not results in changes in completeness due to the relatively small number of missed events. Only a detailed analysis can reveal the real changes in completeness that remain undiscovered when applying the classical G-R methods, as documented by Nanjo et al. (2010).
- On the northern borders of Greece to other countries, one can clearly observe a strong decline in completeness, at some places even affecting the completeness levels on the territory of Greece. It has become increasingly clear and documented that networks need to include stations from adjacent countries in the triggering mechanisms. Often networks retrieve data from foreign stations only once an earthquake has been detected. While this approach can decrease the location uncertainty, it has no influence on the completeness as it is based on the triggering to start the location procedure.

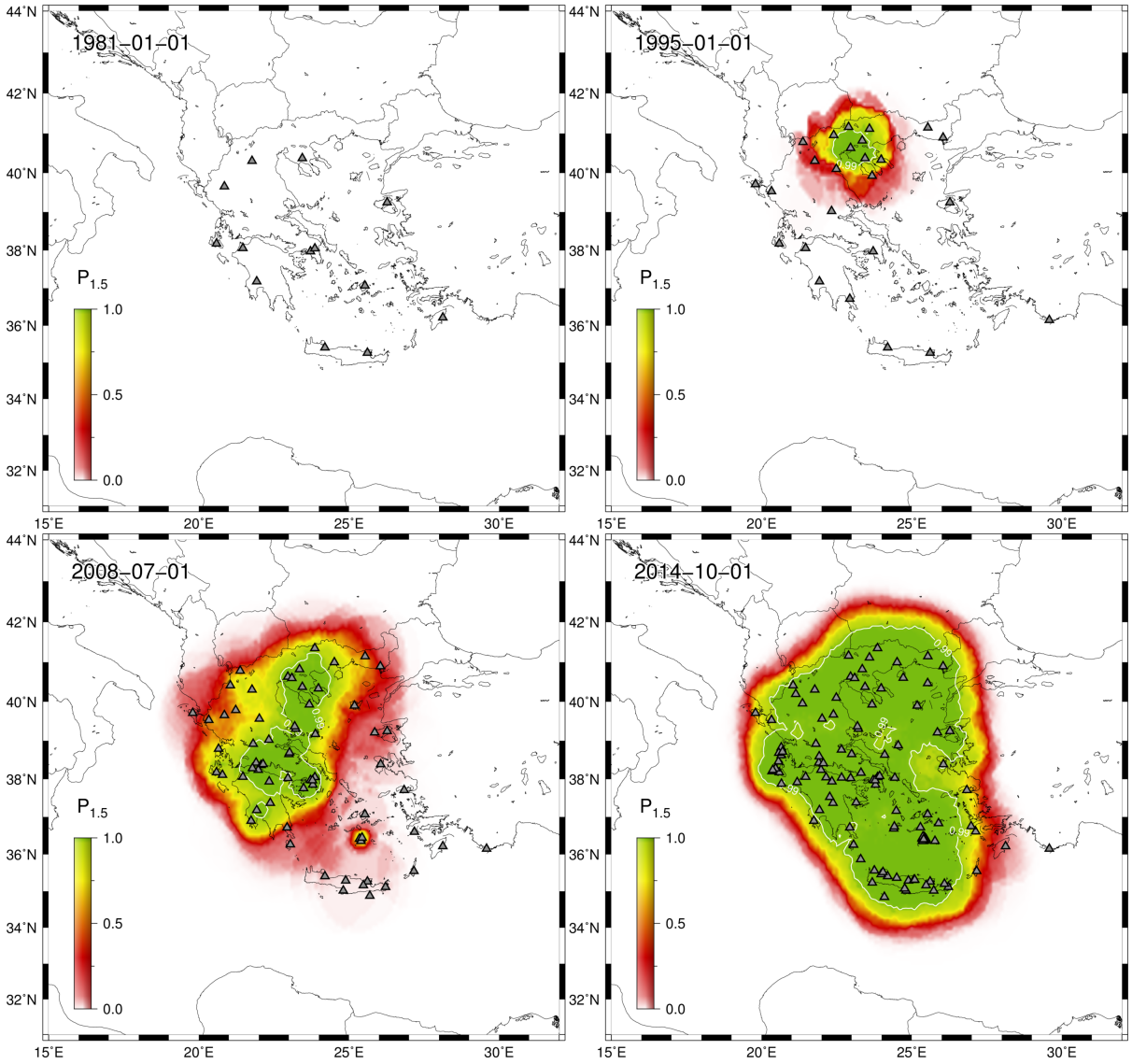

Figure 3. Detection probabilities of earthquakes of magnitude 1.5 for four different dates (1 January 1981, 1 January 1995, 1 July 2008, 1 October 2014). All stations operational on the respective dates are marked with grey triangles.

- Because the completeness mainly depends on the density of stations, it would be helpful to cover some areas with ocean-bottom seismometers to ensure a more homogeneous recording quality, in terms of completeness and location uncertainty.
- All of the above items need to be considered when running statistical studies, in particular ones involving small-magnitude events. Only rigorous completeness studies over space and time can show the gaps in recording that will likely result in underestimated rates of smaller events.
- To improve the quality of these types of analyses, networks should store the automatic picks that triggered the location procedure. Some networks only store the post-processed manual picks which can give a different picture of the recording capabilities of each station, resulting in biased completeness estimates and subsequently in wrong rate estimates.
- To foster more research using seismic-catalogue data, networks should make all information, in particular about the data processing, openly available. Often, only the final catalogue products are available.

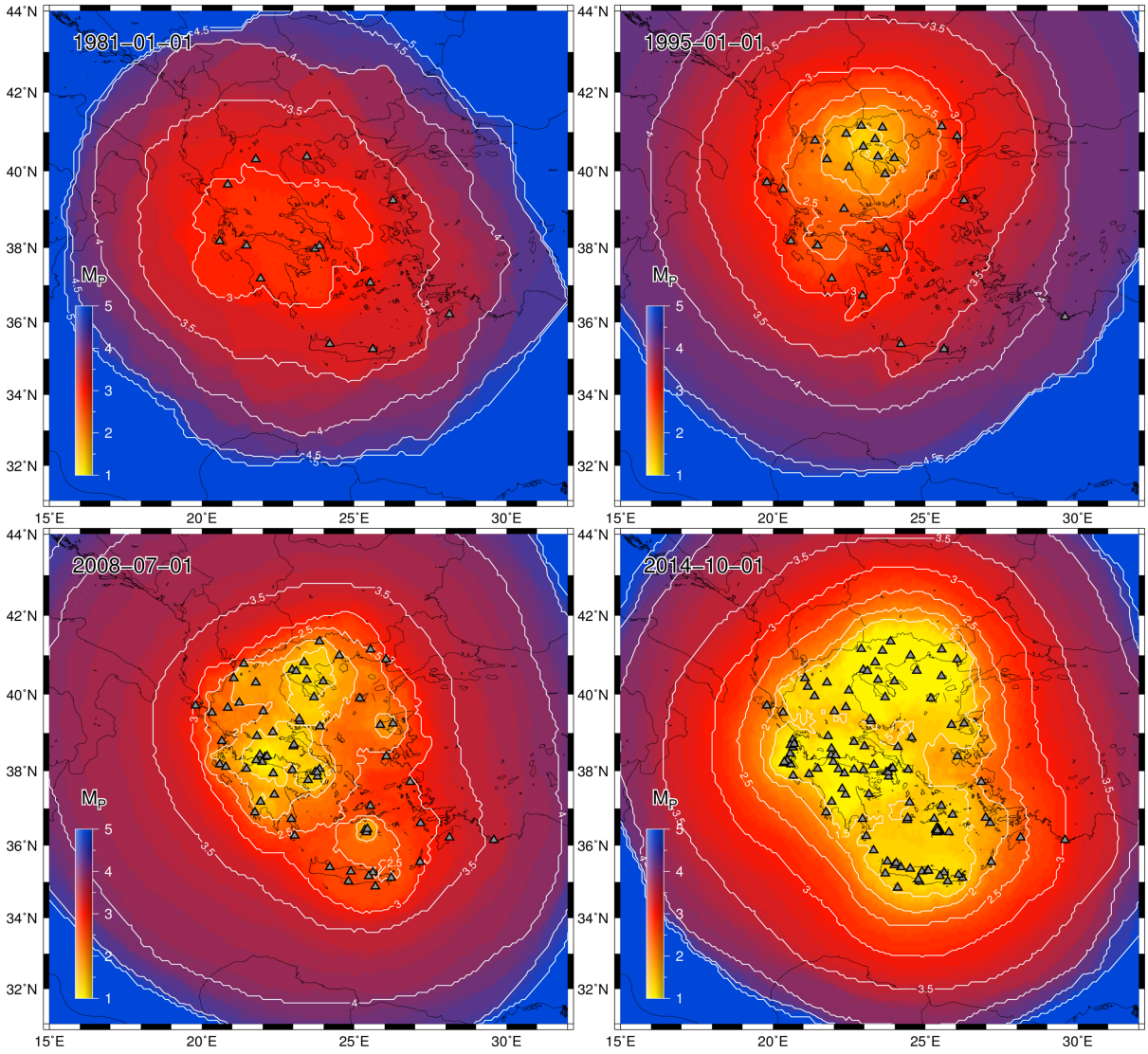

Figure 4. Completeness magnitudes for four different dates (1 January 1981, 1 January 1995, 1 July 2008, 1 October 2014). All stations operational on the respective dates are marked with grey triangles.

- Europe is in desperate need of an uniformly created and homogeneous catalogue that should be routinely created by one entity that has real-time access to all stations in Europe. Only such a homogeneous processing will create a high-quality catalogue for all of Europe with a homogeneous magnitudes and without inconsistencies between different territories.

4. Analysis of network performance at the regional scale: large data sets and low magnitude stress-drop analysis

4.1. Motivation

The development of dense network to monitor specific fault or fault system (e.g. Near Fault Observatories- NFO) allow to lower locally the detection threshold. At the same time, when standard installations are considered (seismic sensors located at the Earth surface), attenuation effects cast a limit for the retrieval of high frequency source parameters (Abercrombie 1995; Abercrombie et al. 2017; Kwiatek and Ben-Zion 2016; Deichmann 2017, 2018). Target of this study is to evaluate the magnitude threshold for the source parameters of small earthquakes. In order to estimate a minimum magnitude threshold for the earthquake size, we generate synthetic spectra considering the source and station distributions of a data set compiled for central Italy where a very dense station coverage is available. The data set includes a large amount of earthquakes recorded in the last decade, in particular the 2016-17 sequence (Bindi et al. 2018; Bindi et al. 2020). We first generate synthetic spectra by convolving standard spectral models for source, source-to-site propagation, and site-specific attenuation effects, considering the data availability and quality of the central Italy data set. Then, we applied a spectral decomposition approach to isolate the source contribution from attenuation and site effects and, in turn, to estimate the source parameters. This virtual experiment allow us to identify first order thresholds for the reliability of the source parameters (seismic moment, corner frequency and stress drop) in central Italy. In particular, we observe an increase of the variability of the residual distributions starting from about magnitude 3 and, below magnitude 2.3, systematic biases started to affect the parameters; below magnitude 1.8, the biases could be strong enough to make the source parameters unreliable. We also test the impact of reducing the very dense coverage available for the epicentral area of the 2009 and 2016 sequences by removing a given amount of stations.

4.2. Data and synthetics

We generate synthetic spectra for the source-station geometry of a data set compiled for central Italy (Bindi et al. 2020). We consider stations of the IV (INGV) and IT (Italian Department of Civil Protection-DPC) seismic networks, selecting both velocimetric (HH, EH) and accelerometric (HN, HG) channels. We consider a set of 4111 earthquakes in the moment magnitude range 1.5-6.5, recorded in central Italy between 2009 and 2019, including the 2009, Mw 6.3 L'Aquila and the 2016, Mw 6.2 Amatrice and Mw 6.5 Norcia sequences (Figure 1). The selected data set is composed by almost 400000 waveforms recorded by 373 stations. About 50% of the stations recorded at least 160 earthquakes and about 50% of the earthquakes has at least 20 records. The hypocentral distances span the range 5-150 km, with about 40% of the data recorded at hypocentral distances < 30 km (Figure 2). Magnitudes below 2 provide recordings mainly at distances <40 km (the median of the hypocentral distances for this magnitude range is 24 km) whereas magnitudes larger than 5 are mainly recorded at distances > 40 km with median distance at 67 km (Figure 3).

Figures 2 and 3 also show the distributions obtained by removing either the 25 (white) or 60 (green) most contributing stations for distances < 40km. The decimated data sets are used to check the impact of the network density over the spectral decomposition results. Figure 4 compares the network density of the original data set (red) and the one where 60 stations are removed (green) in terms of Voronoi diagram density in the epicentral area. Computing the cumulative distribution function of the areas of the Voronoi cells, 50% of the cells have an area smaller than 53 km^2 and 79 km^2 for the complete and decimated data set, respectively.

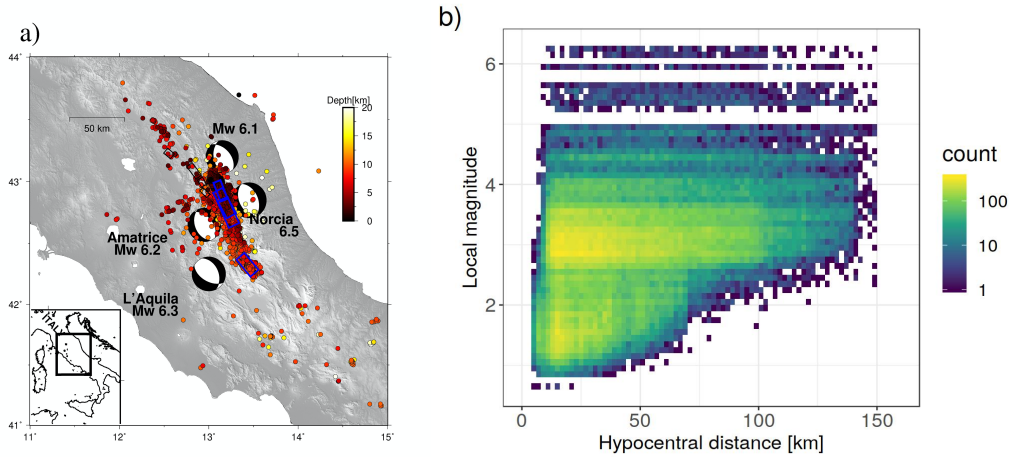

Figure 1. Central Italy data set used to guide the generation of synthetic spectra. a) Earthquake locations, colour coded by hypocentral depths; b) local magnitude versus hypocentral distance density plot in terms of absolute number of recording per scenario.

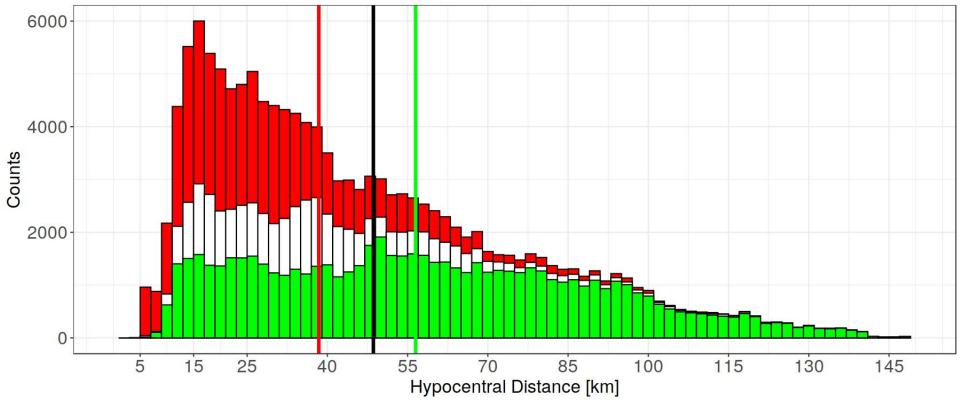

Figure 2. Histograms for the number of recordings per distance bin considering the whole data set (red) and the two other data sets obtained by removing either the 25 (white) or 60 (green) most contributing stations at distances < 40 km.

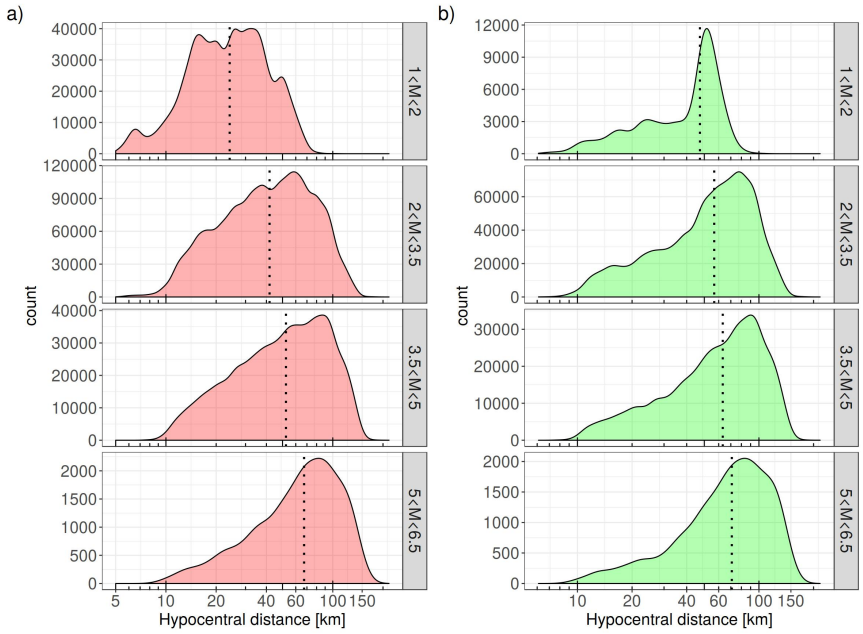

Figure 3. Distance sampling for different magnitude ranges considering: a) the whole data set; b) removing the 60 stations most contributing at distances shorter than 40 km (see Figure 2).

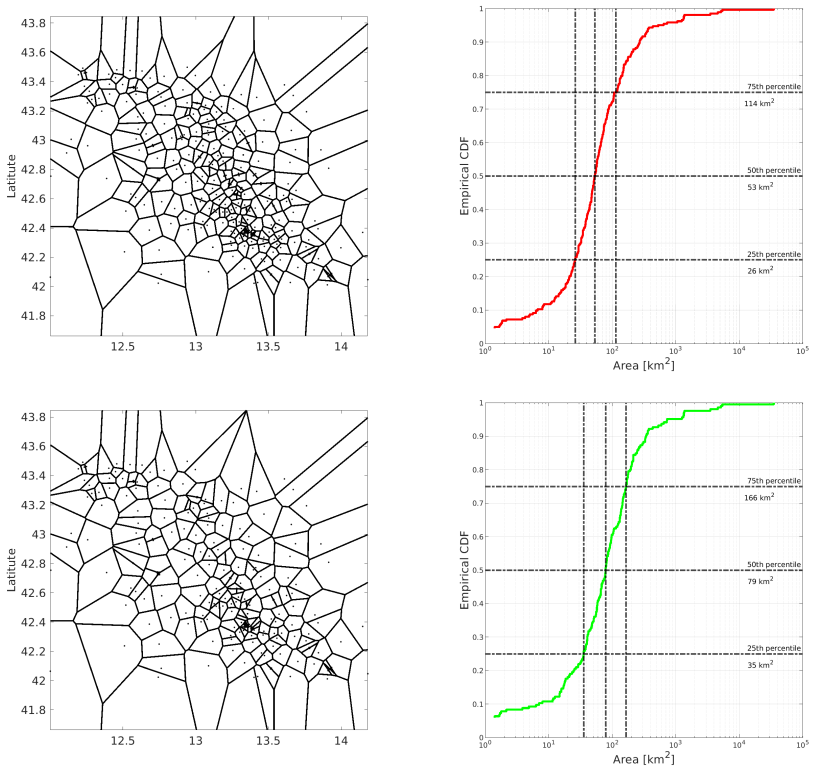

Figure 4. Station density in terms of Voronoi diagrams for the original data set (top) and the data set where 60 stations were removed as in Figure 16 (bottom). In the right panels, the empirical cumulative distribution of the areas of the Voronoi's cells are shown along with some percentiles.

We compute the FAS of S-wave windows selected accordingly to the fraction of cumulated energy and the Fourier Amplitude Spectra (FAS) are smoothed with the Konno and Ohmachi (1998) algorithm (Bindi et al. 2018). For each spectrum, the signal-to-noise ratio (SNR) for 80 frequencies equally spaced in the logarithmic scale within the bandwidth 0.3-30 Hz is evaluated with respect to a pre-event noise window.

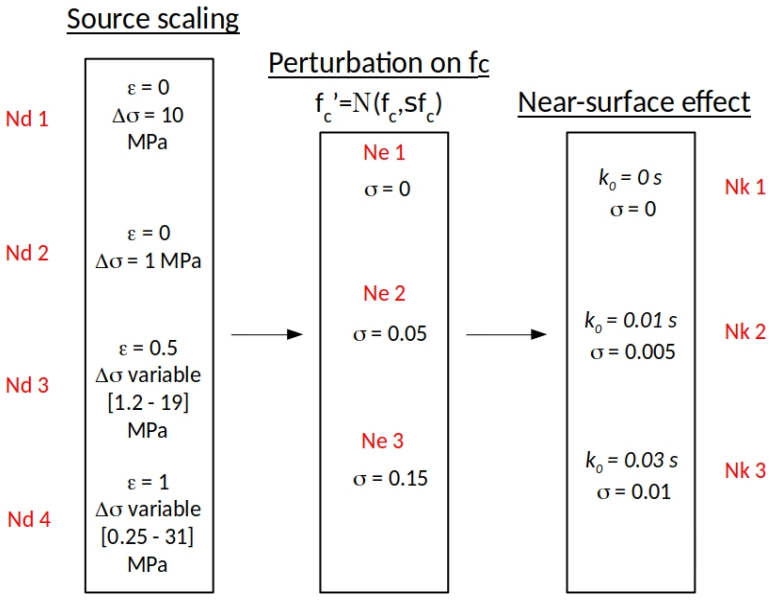

Figure 5. Summary of the models used to generate the synthetic spectra.

We select only spectral amplitudes having SNR ≥ 10 if the frequency is between 0.4 and 15 Hz and SNR ≥ 5 for frequencies outside this range, discarding the whole spectra if less than 75% of frequencies overcome the SNR selection. Finally, the quadratic mean of the horizontal components is computed.

We generate the synthetic spectra using almost the same design matrix defined by the actual data set and convolving standard models for source, propagation and site effects (Figure 5).

We consider the Brune's source model (Brune 1970, 1971), defined in terms of seismic moment M_0 and corner frequency f_c and generating different source scaling model for their relationships. In particular, we considered models defined by (Kanamori and Rivera 2004):

$$M_0 \propto f_c^{-(3+\varepsilon)} \tag{1}$$

where $\varepsilon = 0$ corresponds to the self-similarity scaling (constant stress drop, $\Delta\sigma$). We generate data sets of synthetic spectra for different choices of ε and $\Delta\sigma$, where $\Delta\sigma$ is computed as in Eshelby (1957). In particular, we generate two scaling models for ε=0, with constant stress drop equal to $\Delta\sigma$=1 and 10 MPa, and two models with stress drop variable with magnitude by setting ε=0.5 and ε=1 in equation (1). The logarithm in base 10 of the corner frequencies are perturbed considering three normal distributions with standard deviations σ=0 (referred to as Ne1, where any perturbation is applied), σ=0.05 (model Ne2) and σ=0.15 (model Ne3). Such perturbations add variability to the stress drop distributions while preserving the average scaling relationships. Examples of the constructed source scaling models for different combinations of $\Delta\sigma$ and ε are shown in Figure 6.

The spectral attenuation with distance is modelled considering a piece-wise linear geometrical spreading with break-point at 80 km, where the slope changes from 1 to 0.5, coupled to an anelastic attenuation term with $Q(f)=250\ f^{0.15}$. Regarding the site effects, we consider only the near-surface attenuation

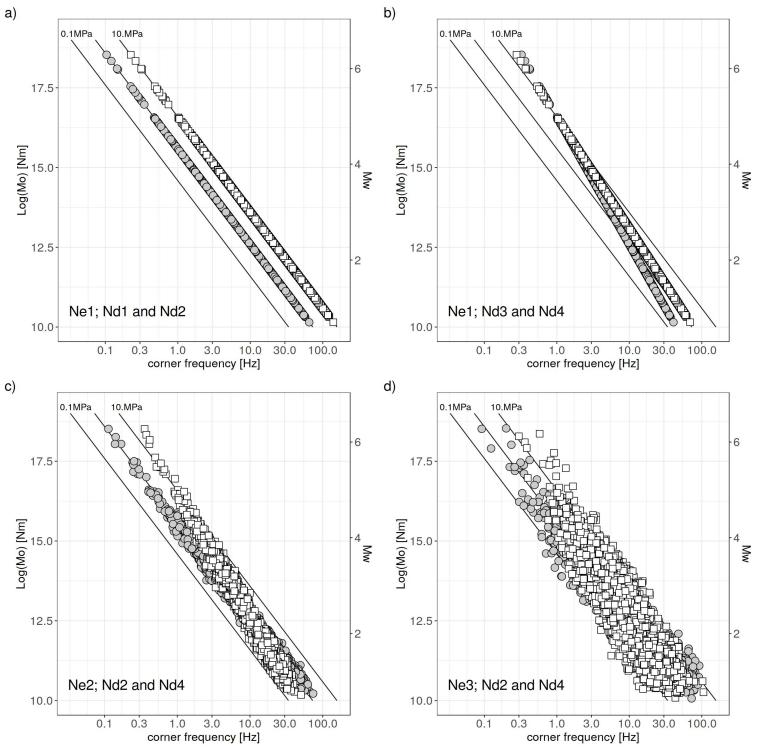

Figure 6. Source scaling models used for generating the synthetic spectra (Figure 5). a) Models with constant stress drop $\Delta\sigma$ equal to 10 MPa (Nd1) and 1 MPa (Nd2), without additional variability on the mean scaling (Ne1). b) Scaling for variable $\Delta\sigma$, considering ε=0.5 (Nd3, white squares) and 1 (Nd4, grey circles) (see equation 5). c) Scaling for models Nd2 and Nd4 adding a normal perturbation with σ=0.05 (Ne2). d) Scaling for models Nd2 and Nd4 adding a normal perturbation with σ=0.15 (Ne3).

effects, which mostly impact on our ability to retrieve high frequency source information from recordings. We used three different distributions of k_0 (Anderson and Hough, 1984): k_0=0 (no site effects, Nk=1); a normal distribution with mean 0.01 s and standard deviation 0.005s (Nk=2); a normal distribution with mean 0.03 s and standard deviation 0.01 s (Nk=3). Figure 7 shows the generated distribution of k_0 values. The synthetic spectra are not corrupted with random noise but we use the outcomes of the SNR analysis performed over spectra of actual recordings. In particular, for each synthetic spectrum, we analyse only those frequencies for which the SNR of the corresponding real spectra is larger than 10 for frequencies within the range 0.4-15 Hz, and larger than 5 for frequencies outside this range. With this approach, we assess the GIT performance considering the same amount of information used for the analysis of real data.

4.3. Results

The spectral decomposition approach applied in this study is known as generalized inversion technique (GIT) (e.g., Bindi et al. 2018). The Fourier amplitude spectra (FAS) of the S-waves are modelled as product (convolution) among source, propagation and site spectra. We apply the GIT in the non-parametric form where the factors are not bound to follow any a-priori functional form and tables of spectral values are retrieved for each source and site amplification spectra and for the spectra attenuation with distance. In the GIT approach, the computed FAS are described as:

$$logFAS_{ij}(f) = logP_{ij}(R, f) + logS_i(f) + logZ_j(f) \quad (2)$$

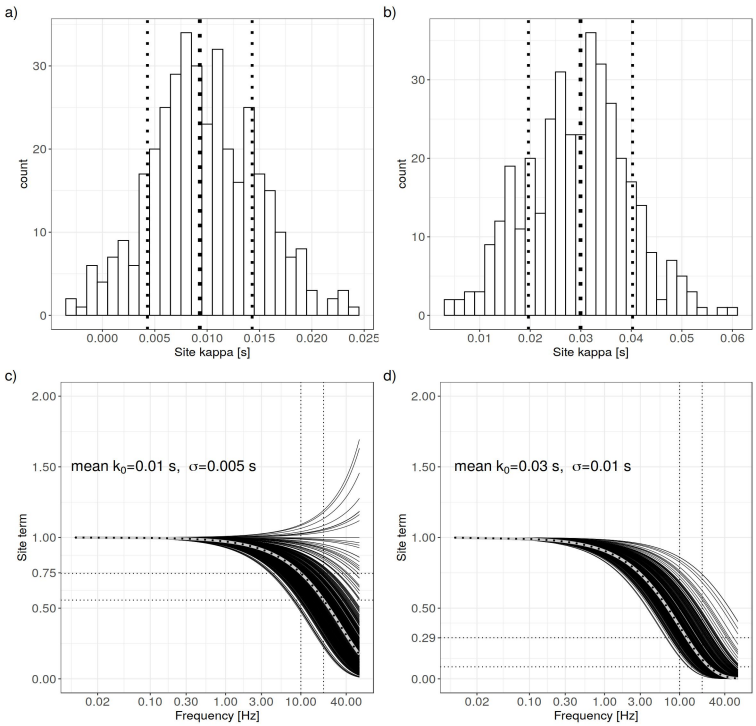

Figure 7. Site term used for generating the synthetic spectra. a) Distribution of k_0 for the case Nk2 (i.e., average k_0=0.01 s and σ=0.005 s). b) Distribution of k_0 for the case Nk3 (i.e., average k_0=0.03 s and σ=0.01 s). c) Site term computed for the distribution in panel a). d) Site term for panel b). In panels a) and b), vertical dotted lines indicate the mean and the standard deviation of the numerical k_0 distributions; in panels c) and d), dashed grey lines indicate the site term for the mean k_0.

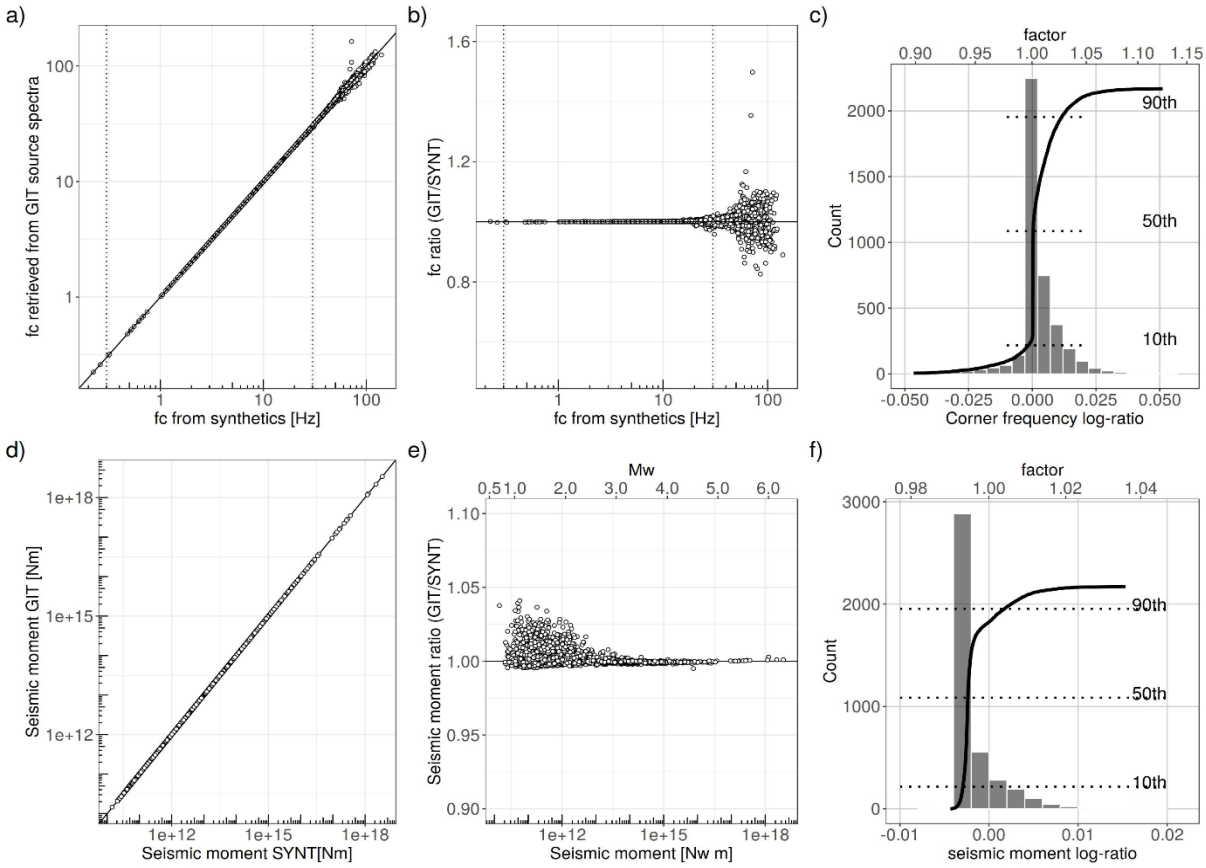

Figure 8. Corner frequency (top) and seismic moment (bottom) results relevant to the simulations Ne=1, Nd=1, Nk=1 (Figure 5), corresponding to constant $\Delta\sigma$ (Ne1) equal to 10 MPa (Nd1) and no site effects (Nk1). a) comparison between fc estimated from the GIT source spectra versus the model values; b) ratio of the retrieved corner frequency and the model one versus the modelled ones; c) histogram and cumulative distribution of the logarithm of the retrieved over modelled corner frequency ratios. In panels a) and b), the vertical dotted lines at 0.3 and 30 Hz indicate the spectral bandwidth used for the fitting the source spectra. In panels d), e) and f) the same analysis are repeated for the seismic moment.

where $FAS_{ij}(f)$ is the observed spectral amplitude at frequency f associated to event i registered at station j; P_{ij} the spectral attenuation for hypocentral distance R equal to R_{ij}; $S_i(f)$ is the source spectra of event i at frequency f; $Z_j(f)$ is the site amplification term for station j at frequency f. The distance range from 5 to 100 km is discretized into intervals 2.5 km wide, and distances from 100 to 150 km into intervals 5 km wide. The he over-determined system of equations generated by equation (2) is solved in a least-squares sense under some constrained introduced to removed trade-offs among the factors. We assume a reference distance at which LogP is set to zero (that is, the sources are scaled at the reference distance, generally assumed as smaller as possible compatible with the actual data sampling) and a reference site condition such as constraining to one the average amplification of all stations, or of a subset of stations (typically those of stations installed on rock). Details are available in Bindi et al. (2018, 2020). Therefore, synthetic FAS are generated using the parametric models for the three factors in equation (2) and then inverted without considering any specific functional forms for the unknown terms. Once the source, attenuation and site terms are isolated, the source and attenuation parameters are extracted from the non-parametric solutions using the same parametric models used to generate the synthetics. As consequence of this choice, we neglect the epistemic uncertainty affecting the model selection and the uncertainties affecting the retrieved source parameters should be considered as a lower bound for real data analysis (analysis with real data cannot produce better estimates).

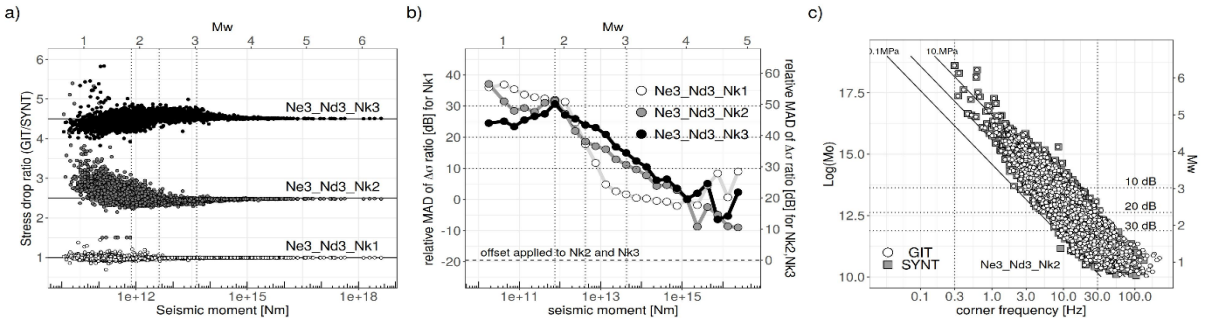

Figure 9. Results for different k_0 models: Nk1 corresponds to k_0=0; Nk2 corresponds to average k_0=0.01s with sigma 0.005s; Nk3 corresponds to average k_0=0.03 s with sigma 0.01s (see Figure 5). a) Retrieved over synthetic stress drop ratios versus seismic moment for the cases Ne3_Nd3 (ε=1 with variability over fc values with σ=0.15, see Figure 5) and the three k_0 models; the results for Nk2 and Nk3 are shifted upward of 1.5 and 3.5 for graphical reasons. b) Relative median absolute deviance (MAD) of the distributions shown in panels a), considering equation (4); values for Nk1 model are shown on the left vertical axis, those for Nk2 and Nk3 models on the right vertical axis. The value of the offset δ applied in equation (4) is shown as horizontal dotted line. c) Comparison between retrieved (white circles) and synthetic (grey squares) scaling between seismic moment and corner frequency for the model Ne3_Nd3_Nk2.

Figure 8 compares the synthetic and GIT results in terms of corner frequency and seismic moment, considering the case Ne=1, Nd=1, Nk=1 (i.e., constant $\Delta\sigma$=10 MPa without k_0 effects, see Figure 5). In this case, the finite bandwidth effects are only related to Q and they are common to all events, although the limitations are distance dependent. Figure 7a and 7d shows that on average both the corner frequencies and seismic moments are well retrieved over a broad magnitude range, confirming that the GIT was able to resolve the correct non-parametric source spectra.

The good performances for events with fc above 30 Hz are ascribed to the fact that fc is affecting also frequencies below the corner and we are fitting the synthetic data with the true parametric model, without considering epistemic uncertainty. To better emphasize the relative performance of the spectral fitting for events of different size, panels (b) and (e) of Figure 8 show the ratio of the corner frequency and seismic moment with respect to the true values. Panel (b) shows that the retrieval of f c starts to be affected by limited-bandwidth effects when fc is approaching the upper limit of 30 Hz from below, although only above 40 Hz the dispersion of the ratios becomes evident. Please note that, as shown by the histograms in panels (c) and (f), for more than 90% of the events the parameters can be retrieved within a few percent of relative error; anyway, in the analysis of real data, errors could be larger due to the presence of model errors. Therefore, in the following we do not concentrate our attention on the absolute errors but on their variability when decreasing the earthquake size. The seismic moment shows a slight underestimation and the ratios show a larger dispersion below magnitude 2.5.

When the near-surface attenuation effects are included in the simulations, station-specific low pass filters are applied on the ground shaking, being the filtering effects controlled by k_0. As shown in Figure 7, the model Nk2 (average k_0 = 0.01 s) reduces on average the spectral amplitude at 10 Hz of 25%; for the case Nk3 (average k_0 = 0.03 s), the reduction at 10 Hz is as strong as 70%. Therefore, the assessment of the corner frequencies for small events is expected to be strongly hampered by the near surface attenuation.

Figure 9 shows the results for the three k_0 models in terms of stress drop comparison, considering ε=0.5 (Nd3) for the case Ne=3 (where a variability applied to the average source scaling). The stress drop ratios in Figure 9d show that while for k_0=0 we observe an increase of the variability starting for magnitudes below about 2.5, introducing the near surface attenuation k_0 worsen the results below magni-

tude 3 and trends diverging from zero are observed below magnitude 2. Figure 9e quantifies the increase of variability observed in panels (a) and (d) by computing the ratio between the median absolute deviance (MAD) parameter computed for a given k_0 model and the MAD for k_0=0, that is:

$$MAD = median\left[\left|Y_i - median(Y_j)\right|\right] \quad (3)$$

$$relativeMAD = 20\log\frac{MAD(k_0)}{MAD(k_0 = 0)} + \delta \quad (4)$$

where Y refers to the residuals computed as difference between retrieved and synthetic source parameters and MAD in equation (3) is computed binning the logarithm of the moment over intervals 0.25 Log(Mo) units wide. In equation (4), the offset δ is applied to anchor to zero the relative MAD computed for a reference seismic moment. In Figure 9b, the offset applied to the relative MAD is -19.4 dB, corresponding to the MAD of Nk2 model evaluated in the magnitude range 4-4.5.

Figure 9b shows that, whereas the MAD for k_0=0 increases below magnitude 3 as consequence of the Q attenuation discussed for Figure 6, the relative MAD for the Nk2 and Nk3 models describe a continuously increasing variability of the $\Delta\sigma$ residuals for decreasing magnitude. With respect to the assumed reference value, the relative MAD increases of 10, 20 and 30 dB when the moment magnitude becomes smaller than about 3, 2.3 and 1.8, respectively. If we export these results to the analysis of the central Italy data set, we expect that the uncertainties on the source parameters increase for magnitudes in the range 2.3-3; for magnitudes in the range 1.8-2.3, the uncertainties further increase and biases likely start to affect the results; finally, below magnitude 1.8, the reliability of the results might be strongly reduced due to the attenuation effects related to Q and k_0. Finally, Figure 9c shows that, although $\Delta\sigma$ estimates for magnitudes below 2.3 are less reliable, the average scaling is captured well over almost the entire magnitude range.

The spectral decomposition benefited by the availability of a dense network coverage, especially at short distances from the source. Figure 10 compares the quality of the corner frequencies and stress drop obtained when either 25 or 60 stations are removed, reducing significantly the sampling at distances shorter than 40 km (see Figures 2 and 3). Since the settings applied for the inversion are the same for all data sets (e.g., minimum number of stations per event) and since small earthquakes are mainly recorded at short distances (Figure 3), the number of events in the decimated data sets is smaller than in the original data set, in particular for small events (Figure 3, right). Therefore, the results are compared considering only the 2140 earthquakes common to all three cases. Figure 10 shows that the performances of the GIT inversion for small events is worsening when the short distances are less sampled. For the case when 60 stations are removed, the dispersion of the corner frequency ratios is larger than for the case of complete data set, in particular above 10 Hz. In general, we see a worsening of the results below magnitude 2.5.

4.4. Conclusions

The reliability of the source parameters for small events is relevant for many applications ranging from near fault monitoring to detect the emergency of transients to monitoring applied in the context of anthropogenic hazard. We investigated the reliability of the source parameters estimated in the moment magnitude range 1.5-6.5 considering the network layout and the data availability in central Italy. We considered a virtual experiment where synthetic spectra were generated numerically for the same matrix design of the central Italy data set. We used a spectral decomposition approach to factorize the Fourier spectra of S-wave windows into source, propagation and site effects, using the synthetic spectra as a benchmark to evaluate the reliability of the results and, in particular, the resolution limits towards

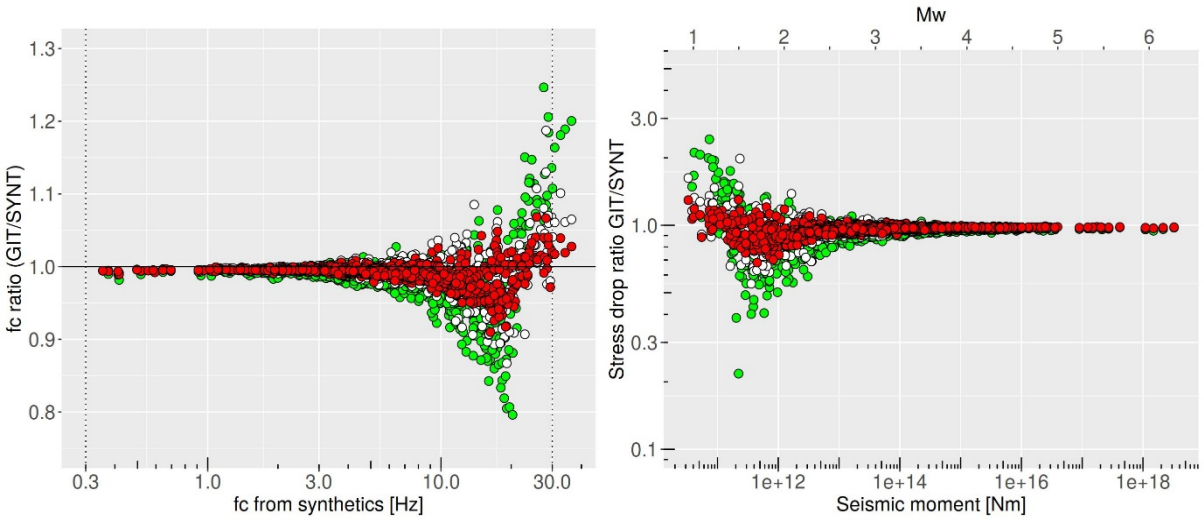

Figure 10. Results of the analysis performed removing either 25 (white) or 60 (green) stations (see Figures 2 and 3) for the case Ne=2, Nd=4 and Nk=2 (see Figure 5).

small magnitudes. The main outcomes of the analysis with synthetic spectra performed in this study are:

1. the large redundancy in the earthquake and station sampling, and the good azimuthal and distance distributions in particular at short distances, allowed us to retrieve reliable non-parametric source spectra over the analysed magnitude range;
2. below magnitude 3, we observed an increase of the variability of the source parameters residuals as consequence of whole-path attenuation effect; anyway, only below magnitude 2.3 systematic biases started to affect corner frequencies approaching the upper limit of the analyzed bandwidth, due to large stress drop values; the source parameters can be significantly biased below magnitude 1.8;
3. the site-specific near-surface attenuation, modelled through the kappa parameter, plays a strong role in limiting the retrieval of reliable corner frequencies for small events.

5. Analysis of network performance at the mine scale

5.1. Description of the LUMINEOS network

The LUMINEOS network is today an installation of 17 stations equipped with broadband GEOSIG seismometers and 10 stations equipped with GEOSIG accelerometers to record all types of seismic activity in the network area (Figure 1b). The specific task of LUMINEOS is to monitor induced seismicity as caused by mining activities of RUDNA Deep Copper Mine. Rudna is part of the Legnica-Głogow-Copper-District in SW Poland and characterized by a high seismicity rate producing frequently events of up to magnitude 4. Although an in-mine seismological network exists which is operated by the owners of the mine, the only option to get sufficient data for scientific purposes was to install a surface network capable of registering a broad range of seismic signals due to mining activity, induced seismicity and potential triggered tectonic events. One of the crucial challenges of this network therefore is to be able to record events from micro seismicity to magnitude 4. The network started in 2013 with the operation of 4 short-period seismological stations until it perceived its actual layout in 2017. The network is owned and operated by IG-PAS, Department of Seismology.

5.2. Analysis of LUMINEOS data with BackTrackBB and PyMPA software

The recorded data from LUMINEOS network is transferred using the GSM standards to IG-PAS datacenter. Then, in the central site in Kraków, the daily processing of the data is carried out. This daily routine work results in up-to-date seismological catalogues for the network area which are available through

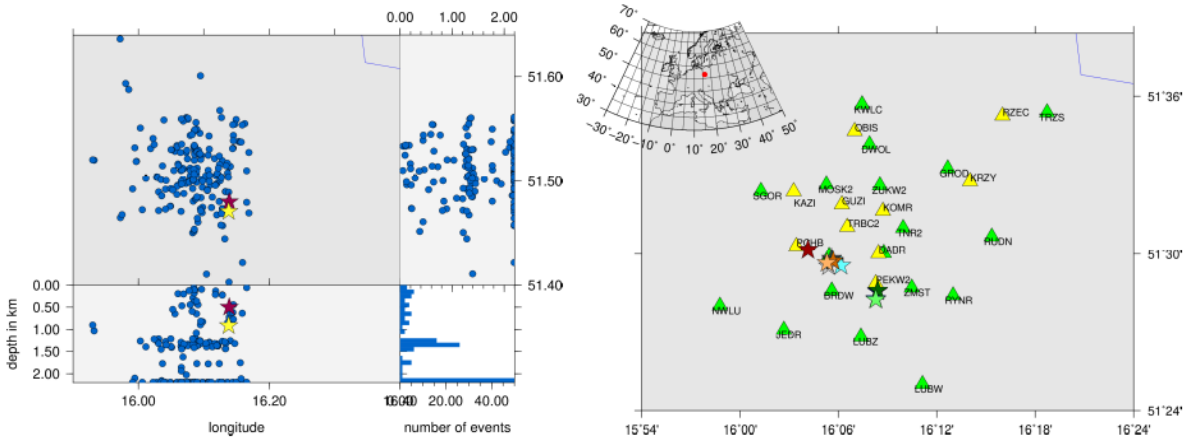

a) b)

Figure 1. a) is showing the spatial distribution of half an hour of data after the 20180915 M4 mine collapse. Red stars mark the main shock as determined by the routine seismological catalogues, yellow stars mark the location by BTBB. b) shows the LUMINEOS station distribution (green triangles are BB stations, yellow triangles are accelerometers). Red star shows a detonation one hour before the major mine collapse. The green stars (dark: in-mine system, light: LUMINEOS) show the location of the first aftershock which is exactly on top of the location (blue, can not be seen) for the main shock. The cluster between the red star and the green stars mark the aftershock 1 to 4 and their respective locations. Darker colours are assigned to the in-mine system, lighter colours are assigned to corresponding LUMINEOS plus BTBB calculations. These tightly clustering locations clearly show the similarity of solutions from the in-mine system and LUMINEOS+BTBB.

the IS-EPOS Platform for Induced Seismicity and Anthropogenic Hazard: https://tcs.ah-epos.eu/login.html.

In order to investigate the possibility of supporting the daily routine catalog with additional detections and locations from automated picking software, we applied BackTrackBB (BTBB, Poiata et al. 2016, Poiata et al., 2018) and PyMPA (Vuan et al. 2018) to LUMINEOS data. The major observations and perceptions from this data processing are the following:

- we can observe a large variety of seismic signals from larger mining collapses, to smaller induced seismic events, mining activities like production and de-stress blastings or machinery noise
- blasting delay intervals from 25ms to 4000ms can be corroborated in the data records
- provoked event signal can be clearly distinguished from blasting signals by their characteristic form (Palgunardi et al. 2019)
- the spatial distributions of seismic events line out mine features like major galleries and actual working areas, shafts, and assumed vertical fault strands (see Figure 1a).

Through these observations we deduce that the LUMINEOS surface network is capable to monitor mining activities and resulting induced or triggered seismicity for scientific studies such as earthquake physics. The larger amount of detected and located events through the application of BTBB and PyMPA software supports the use of statistical methods. For comparison of results obtained for epicentral locations of events from the in-mine system to results from LUMINEOS data, see Table 1. This comparison can also be seen in Figure 1b. The colours given in the last column of the table correspond to the colours of the stars in the figure.

Table 1. Comparison of calculated locations from the in-mine system to LUMINEOS surface network of a blasting event (B), a mine collapse main shock (MC), and several aftershocks (AS). The colours in the last column correspond to the stars in Figure 1b marking the respective events.

Origin time		Latitude		Longitude	
in-mine	surface	in-mine	surface	in-mine	surface
17:37:32 B	15:37:56		51.50235		16.06892 red
18:35:14 MC	16:35:14.3	51.47596	51.47119	16.13959	16.13791 blue
18:37:59 AS1	16:38:06.4	51.47661	51.47065	16.14001	16.13784 green
21:52:08 AS2	19:52:07.7	51.49701	51.49199	16.09292	16.09003 grey
22:24:16 AS3	20:24:21.0	51.49552	51.49249	16.09393	16.10251 turk.
22:38:45 AS4	20:38:46.5	51.49517	51.49410	16.09462	16.08830 oran.

5.3. Magnitude of completeness study for LUMINEOS

Using the data from the routine seismological catalogue calculated from data of the LUMINEOS network, we carried out a magnitude of completeness (Mc) study using the methodology developed by Schorlemmer and Woessner (2008). This is based on a moment magnitude calculation for each event supported by the use of the software SWIP4 and LocSAT, which are the routine tools for detection, location and magnitude estimation of events in the Seismological Center in Kraków. Firstly the probability of an event detection for a given range of magnitudes and distances was calculated for each seis-

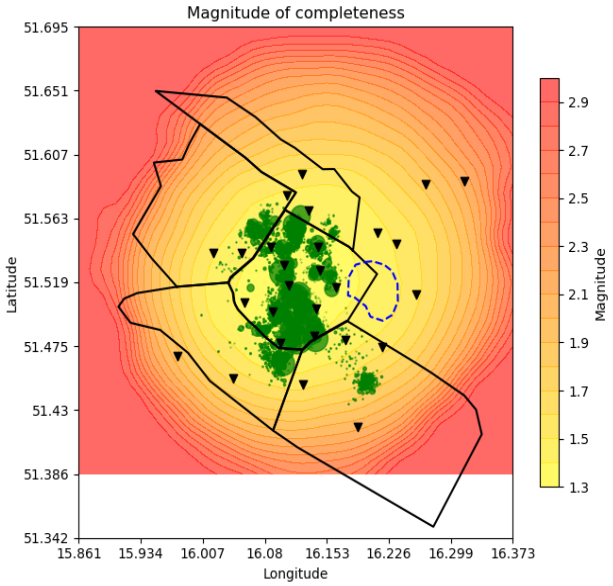

Figure 2. Spatial distribution of the magnitude of completeness Mc from the seismological routine catalogue based on a moment magnitude Mw scale estimated within a period between 07.2016 - 07.2019. The lowest Mc can be found in the central part of the network which covers the area of Rudna Copper Mine. The outlines of the mine are shown by the black lines. The central almost square form images the outer limits of Rudna mine while neighbouring mines are also shown. The blue dashed line indicates boundaries of Żelazny Most tailings pond. The epicentres are shown as a green circles with sizes proportional to their moment magnitude.

mic station. Then, using basic combinatorial procedure, the detection probability for the given magnitude and hypocentre location was determined. The final result is a magnitude of completeness (Mc) map. The map (Figure 2) shows the lowest possible magnitude which can be correctly detected with the probability of 99 % with respect to the network layout. As it could be expected, the lowest Mc can be found in the central part of the network going down to Mc = 1.3 of the moment magnitude. This study will be repeated for the BTBB catalogue when magnitude calculations are available.

5.4. Conclusions and lessons learned

In this deliverable, we have addressed the problem of national and regional network performance and the influence of the network characteristics (geometry, instrumentation) on the physical and statistical understanding of earthquake processes.

These analyses show the relevance of opening the data in a common format (EIDA). It is now possible to have a significant number of earthquakes recorded by different national networks in Europe. This possibility opens the way to a European characterization of the properties (e.g. stress-drop) of small earthquakes (M<3) not studied by the global networks.

These analyses have shown however that it is critical to develop procedures and methods to control data quality. Systematic testing of the calculated residuals between the amplitudes of the European earthquake records and the attenuation models developed in chapter 1 is one of the possible methods. This method makes it possible to detect errors linked in particular to changes in equipment and associated variations in instrumental response and check the consistency between regional network inventories and European inventories.

The discussions and analyses performed in this task show the need to develop an uniform and homogeneous European catalogue that should be routinely created by one entity that has real-time access to all stations in Europe. Only such a homogeneous processing will create a high-quality catalogue for all of Europe with a homogeneous magnitudes and without inconsistencies between different territories. The work developed in the chapter 1 is a first attempt in this direction.

At the national level, temporal losses of completeness due to station outages should be detected and documented by the networks. To improve the quality of these types of analyses, networks should store the automatic picks that triggered the location procedure (and not only) the post-processed manual picks which can give a different picture of the recording capabilities of each station. More generally, networks should make all information, in particular about the data processing, openly available. Often, only the final catalogue products are available.

Because the completeness mainly depends on the density of stations, it would be helpful to cover some areas with ocean-bottom seismometers to ensure a more homogeneous recording quality, in terms of completeness and location uncertainty (see also the discussion and suggestion of Deliverables 4.6 and 4.7). Indeed, chapter 3 show clearly that large redundancy in the earthquake and station sampling, and the good azimuthal and distance distributions in particular at short distances, are needed to retrieve reliable non-parametric source spectra for small (M<3) magnitude earthquakes.

This report finally shows that new and dense networks in mines allow the observation of a large variety of seismic signals from larger mining collapses, to smaller induced seismic events, mining activities like production and de-stress blastings or machinery noise

6. References

Abercrombie, RE (1995) Earthquake source scaling relationships from -1 to 5 ML using seismograms recorded at 2.5-km depth. Journal of Geophysical Research 100(12): 24,015-24,036.

Abercrombie RE, Bannister S, Ristau J, Doser D (2017) Variability of earthquake stress drop in a subduction setting, the Hikurangi Margin, New Zealand. Geophysical Journal International 208: 306–320

Anderson JG, Hough SE (1984) A model for the shape of the Fourier amplitude spectrum of acceleration at high frequencies. Bulletin of the Seismological Society of America 74: 1969–1993

Bindi D, Massa M, Luzi L, Ameri G, Pacor F, Puglia R, Augliera P (2014) Pan-European ground-motion prediction equations for the average horizontal component of PGA, PGV, and 5 per cent-damped PSA at spectral periods up to 3.0 s using the RESORCE dataset. Bulletin of Earthquake Engineering 12: 391–430

Bindi D, Spallarossa D, Picozzi M, Morasca P (2020) Reliability of source parameters for small events in central Italy: insights from spectral decomposition analysis applied to both synthetic and real data. Bulletin of the Seismological Society of America, submitted

Bindi D, Spallarossa D, Picozzi M, Scafidi D, Cotton F (2018) Impact of magnitude selection on aleatory variability associated with Ground- Motion Prediction Equations: Part I—local, energy, and moment magnitude calibration and stress-drop variability in central Italy. Bulletin of the Seismological Society of America 108(3A): 1427–1441

Bindi D, Zaccarelli R, Strollo A, Di Giacomo D (2019a) Harmonized local magnitude attenuation function for Europe using the European Integrated Data Archive (EIDA). Geophysical Journal International 218: 519-533

Bindi D, Zaccarelli R, Strollo A, Di Giacomo D (2019b) Attenuation coefficients and station corrections for harmonized local magnitude scales in Europe. V. 1.0. GFZ Data Services, doi: 10.5880/GFZ.2.4.2019.003

Bragato PL, Tento A (2005) Local magnitude in Northeastern Italy. Bulletin of the Seismological Society of America 95: 579–591

Brune JN (1970) Tectonic stress and the spectra of shear waves from earthquakes. Journal of Geophysical Research 75: 4997–5009

Brune JN (1971) Correction. Journal of Geophysical Research 76(20): 5002

Deichmann N (2017) Theoretical basis for the observed break in ML/Mw scaling between small and large earthquakes. Bulletin of the Seismological Society of America 107(2): 505

Deichmann N (2018) The relation between ME, ML and Mw in theory and numerical simulations for small to moderate earthquakes. Journal of Seismology 22: 1645-1648

Di Bona M (2016) A local magnitude scale for crustal earthquakes in Italy. Bulletin of the Seismological Society of America 106: 242–258

Eshelby JD (1957) The determination of the elastic field of an ellipsoidal inclusion, and related problems. Proceedings of the Royal Society A 241(1226): 376-396.

Hutton LK, Boore DM (1987) The ML scale in Southern California. Bulletin of the Seismological Society of America 77: 2074–2094

Kanamori H, Rivera L (2004) Static and dynamic scaling relations for earthquakes and their implications for rupture speed and stress Drop. Bulletin of the Seismological Society of America 94 (1): 314-319

Konno K, Ohmachi T (1998) Ground-motion characteristics estimated from spectral ratio between horizontal and vertical components of microtremor. Bulletin of the Seismological Society of America 88(1): 228–241

Kotha SR, Bindi D, Cotton F (2017) From ergodic to region- and site-specific probabilistic seismic hazard assessment: method development and application at European and Middle Eastern sites. Earthquake Spectra 33: 1433–1453

Kwiatek G, Ben-Zion Y (2016) Theoretical limits on detection and analysis of small earthquakes. Journal of Geophysical Research Solid Earth 121(8): 5898-5916

Luckett R, Ottemöller L, Butcher A, Baptie B (2018) Extending local magnitude ML to short distances. Geophysical Journal International 216: 1145–1156

Nanjo KZ, Schorlemmer D, Woessner J, Wiemer S, Giardini D (2010) Earthquake detection capability of the Swiss Seismic Network. Geophysical Journal International 181: 1713-1724

Poiata N, Satriano C, Vilotte J-P, Bernard P, Obara K (2016) Multi-band array detection and location of seismic sources recorded by dense seismic networks. Geophysical Journal International 205: 1548-1573

Poiata N, Vilotte J-P, Bernard P, Satriano C, Obara K (2018) Imaging different components of a tectonic tremor sequence in southwestern Japan using an automatic statistical detection and location method. Geophysical Journal International 213: 2193-2213

Savage MK, Anderson JG (1995) A local-magnitude scale for the western great basin-eastern Sierra Nevada from synthetic Wood-Anderson seismograms. Bulletin of the Seismological Society of America 85: 1236–1243

Schorlemmer D, Hirata N, Ishigaki Y, Doi K, Nanjo KZ, Tsuruoka H, Beutin T, Euchner F (2018) Earthquake Detection Probabilities in Japan. Bulletin of the Seismological Society of America 108(2): 702–717

Schorlemmer D, Mele F, Marzocchi W (2010) A Completeness Analysis of the National Seismic Network of Italy. Journal of Geophysical Research 115: B04308

Schorlemmer D, Woessner J (2008) Probability of Detecting an Earthquake. Bulletin of the Seismological Society of America 98(5): 2103-2117

Spallarossa D, Bindi D, Augliera P, Cattaneo M (2002) An ML scale in northwestern Italy. Bulletin of the Seismological Society of America 92: 2205–2216

Vuan A, Sugan M, Amati G, Kato A (2018) Improving the Detection of Low-Magnitude Seismicity Preceding the Mw 6.3 L'Aquila Earthquake: Development of a calable Code Based on the Cross Correlation of Template Earthquakes. Bulletin of the Seismological Society of America 108(1): 471–480

Zaccarelli R (2018) Stream2segment: a tool to download, process and visualize event-based seismic waveform data. v. 2.7.3. GFZ Data Services, doi:10.5880/GFZ.2.4.2019.002

Zaccarelli R, Bindi D, Strollo A, Quinteros J, Cotton F (2019) Stream2segment: an open source tool for downloading, processing and visualizing massive event-based seismic waveform datasets. Seismological Research Letters 90(5): 2028–2038

Liability claim

The European Commission is not responsible for any use that may be made of the information contained in this document. Also, responsibility for the information and views expressed in this document lies entirely with the author(s).